Computational Mechanics
https://doi.org/10.1007/s00466-023-02389-6

ORIGINAL PAPER

A multiphase-field approach to small strain crystal plasticity accounting for balance equations on singular surfaces

Andreas Prahs[1] · Lukas Schöller[1,2] · Felix K. Schwab[5,6] · Daniel Schneider[2,3] · Thomas Böhlke[4] · Britta Nestler[1,2,3]

Received: 30 March 2023 / Accepted: 9 August 2023

Abstract

An implementation of the crystal plasticity theory in the context of the multiphase-field method provides a numerically efficient tracking of evolving grain boundaries, modeled as diffuse interfaces. In literature, several approaches exist for the implementation of the plastic material behavior within the diffuse interface, based on interpolation, homogenization, or the mechanical jump conditions. Among these, only the jump condition approach exhibits an intrinsic relationship to the sharp interface (SI) theory. Therefore, in the work at hand, the implementation of the crystal plasticity theory within the jump condition approach, referred to as phase-specific plastic fields approach (PSPFA), is discussed in detail. The PSPFA is compared to the interpolation approach, referred to as common plastic fields approach (CPFA), using three-dimensional benchmark simulations of a bicrystal set-up. The comparison reveals that the PSPFA and SI coincide convincingly regarding the accumulated plastic slip and the Mises stress. In contrast, a significant deviation of CPFA and SI is observed both quantitatively and qualitatively, not only within the diffuse interface region, but throughout the complete simulation domain. A variation of the interface width illustrates that this observation can be transferred to the normal components of the total strain, even for smaller interface widths. Consequently, a quantitative estimate of the plastic material behavior, which is crucial for the prediction of the dynamic behavior of grain boundaries, is only provided by the PSPFA. The application of the crystal plasticity in the context of PSPFA to more complex microstructures is illustrated with respect to a periodic honeycomb-structure and an octotuple.

Keywords Crystal plasticity theory · Multiphase-field theory · Mechanical jump conditions

✉ Andreas Prahs
andreas.prahs@kit.edu

Lukas Schöller
lukas.schoeller@kit.edu

Felix K. Schwab
felix.schwab@dlr.de

Daniel Schneider
daniel.schneider@kit.edu

Thomas Böhlke
thomas.boehlke@kit.edu

Britta Nestler
britta.nestler@kit.edu

[1] Institute for Applied Materials - Microstructure Modelling and Simulation (IAM-MMS), Karlsruhe Institute of Technology (KIT), Straße am Forum 7, 76131 Karlsruhe, Germany

[2] Institute of Digital Materials Science (IDM), Karlsruhe University of Applied Sciences, Moltkestraße 30, 76133 Karlsruhe, Germany

[3] Institute of Nanotechnology (INT), Karlsruhe Institute of Technology (KIT), Hermann-von-Helmholtz-Platz 1, 76344 Eggenstein-Leopoldshafen, Germany

[4] Institute of Engineering Mechanics, Chair for Continuum Mechanics, Karlsruhe Institute of Technology (KIT), Kaiserstraße 10, 76131 Karlsruhe, Germany

[5] German Aerospace Center (DLR), Institute of Engineering Thermodynamics, Wilhelm-Runge-Straße 10, 89081 Ulm, Germany

[6] Helmholtz Institute Ulm (HIU), Helmholtzstraße 11, 89081 Ulm, Germany

Published online: 04 October 2023

1 Introduction

1.1 Motivation

Regarding the investigation of polycrystalline materials with respect to their plastic material behavior, experimental data and simulations are commonly compared on basis of dislocation densities or the overall mechanical behavior. For a concise and quantitative relevant prediction of the dislocation densities by simulations regarding a comparison with experimental results, especially the understanding of the plastic material behavior at grain boundaries, present in oligo- or polycrystalline materials, is essential. In contrast to classical plasticity theory, cf., e.g., [1, 2], crystal plasticity (CP) theory, cf., e.g., [3], accounts for the underlying crystalline microstructure such as the crystal lattice, and, thus, the slip systems, characteristic of a particular crystal symmetry such as face centered cubic (FCC) crystals, cf., e.g., [4]. At a continuum mechanical level, CP models consider that plastic deformation takes place on the characteristic slip systems, cf., e.g., [5, p. 447], described by the plastic slip. Crystal plasticity theories, entirely based on the plastic slip, still represent phenomenological models of plasticity in contrast to theories focusing on fundamental mechanisms at smaller length scales, directly addressing lattice defects and dislocations, such as as molecular dynamics, cf., e.g., [6–8], discrete dislocation dynamics, cf., e.g., [9–11], continuous dislocation dynamics, cf., e.g., [12–14]. However, the plastic slips can be associated with the corresponding dislocation densities by Orowan's law in an approximative sense, cf., e.g., [15, Eq.(5)], [16, Eq.(3)]. This offers the possibility to compare experimental results with simulations obtained by the CP theory with respect to larger domains up to specimen size, cf., e.g., [17, 18].

1.2 Crystal plasticity in the sharp interface context - recent modeling and applications

In classical continuum mechanics, cf., e.g., [19, pp. 3–4], grain boundaries are commonly modeled as material singular surfaces, cf., e.g., [20]. A theory that accounts for a continuum with a singular surface is briefly referred to as sharp interface (SI) theory, subsequently. Regarding the field of continuum mechnical CP theory in an SI context, recent developements account, e.g., for the modification of the flow rule. Regarding different hardening behavior as well as the incorporation of the dislocation density into the flow rule for the plastic slip, different flow rules are discussed by [21]. Thermally activated dislocation mechanism are accounted for by the constitutive model presented by [22]. Constitutive models based on dislocation densities are presented, e.g., by [16], regarding modeling the formation of dislocation junction. A thermomechanical elasto-viscoplastic constitutive model, that accounts for thermal strains as well as for temperature dependent material parameters, is presented by, e.g., [23] and applied by [24] regarding the prediction of the behavior of aluminum alloys at elevated temperatures. Further recent applications of the CP theory in the context of SIs are given, among others, by the simulation of void growth within HCP crystals [25], fracture [26], fretting fatigue [27], the TWIP effect [28] as well as the TRIP effect [29], and neural networks [30]. Beyond that, the extension of classic CP theories towards (slip) gradient crystal plasticity theories, cf., e.g., [31–33], enables the modeling of the plastic behavior of grain boundaries, cf., e.g., [34–36].

1.3 Motivation for implementation of crystal plasticity in the multiphase-field method

Regarding an evolving microstructure, the tracking of grain boundaries, represented by material singular surfaces, is numerically costly. This issue becomes especially delicate with respect to polycrystals, exhibiting a vast amount of grain boundaries, being subject to movement in case of solid-solid phase transitions, e.g., martensitic transformation. In the context of the multiphase-field method (MPFM), cf., e.g., [37–40], material singular surfaces such as grain boundaries are represented by interfaces of finite thickness, described by order parameters. This provides a numerically highly efficient treatment of the moving interfaces, as no explicit tracking of the interfaces is necessary, cf., e.g., [41]. Thus, the multiphase-field method is widely established for modeling microstructural evolution processes, such as solidification, solid-solid phase transition, growth and coarsening of precipitations, grain growth and martensitic phase transformation, cf., e.g., [37, 39, 42]. The contributions of the driving forces, accounted for by the evolution equation of the order parameter, are clearly affected by the plastic material behavior in terms of the CP. Thus, the implementation of the CP within the MPFM naturally induces a coupling between both. In literature, the combination of CP and the MPFM is often realized by a mere combination of both methods, where a CP simulation is performed in i) the single crystal context in combination with a PFM simulation, e.g., [43] or ii) the SI context before a subsequent PFM simulation that takes into account the results of the CP simulation, cf., e.g., [44, 45]. It is pointed out that the approach presented in the present work goes far beyond such a combination of CP and MPFM.

1.4 Crystal plasticity in the diffuse interface context—recent modeling and applications

Regarding the diffuse interface of finite thickness, different approaches are considered with respect to the implementation of classical CP theory, in literature. These approaches can be mainly assigned to two categories, the interpolation

and the homogenization approaches, cf., e.g., the discussion by [46, 47].

- Regarding the interpolation approaches, the same constitutive material behavior has to be obeyed by each phase allowing for phase-specific material parameters, however not for phase-specific constitutive laws. Within the diffuse interface region, the material parameters are interpolated based on the distribution of the order parameter. This drastically limits the range of applications excluding, e.g., elasto-plastic laminates.
- The homogenization approaches are associated with homogenization methods used to determine effective material properties of heterogeneous materials, cf., e.g., [48–50]. Thus, each phase can exhibit its own constitutive material behavior. Within the diffuse interface, the stresses or strains are computed based on homogenization schemes. Consequently, these approaches obey the constraints imposed by the assumptions made in the context of the corresponding homogenization scheme. Exemplary, approaches that are based on the Reuss bound consider the stresses of each phase to be the same within the diffuse interface region while the same applies to the strains regarding approaches based on the Voigt bound. It might be pointed out that, within the context of (multi)phase-field theory, these approaches are referred to as Voigt-Taylor approximation, respectively as Reuss-Sachs approximation, while [51] proved that both, the Voigt-Taylor and the Reuss-Sachs approximation are actually bounds.
- A rather new, third approach in the multiphase-field method accounts for the mechanical jump conditions in the sense that the balance of linear momentum at a material singular surface as well as the Hadamard condition are fulfilled at each point within the diffuse interface, cf., e.g., [52–55]. This approach, subsequently referred to as jump condition approach, can be seen as an extension of the homogenization approach as it yields the same results as obtained, e.g., by the Voigt and Reuss approach with respect to specific boundary value problems (BVPs), cf., e.g., [52, 56, 57]. If homogenization is applied in a diffuse interface, the orientation of the diffuse interface has to be taken into account. This can be done using a generalized normal vector. Applying the Hadamard condition together with the classical jump condition, as done by [54], delivers such a homogenization scheme being sensitive to the (generalized) normal direction of the diffuse interface and gives an appropriate homogenization approach. It should also be noted that this approach, in contrast to the other approaches, is intrinsically related to the SI theory.

Clearly, within the diffuse interface, the plastic material behavior does not only depend on the plasticity theory considered, but also on the approach applied regarding the implementation. Moreover, regarding, e.g., the homogenization approach, several homogenization schemes are known, affecting the computation of stresses and strains. Also, a variety of interpolation schemes could be used in the context of the interpolation approach. In contrast, there are no different schemes present associated with the jump condition approach, since the jump conditions represent a balance law and a kinematic compatibility condition. Eventually, the choice of some approaches can even lead to an artificial behavior, induced by the plastic heterogeneity due to the active slip systems, within the diffuse interface region. Thus, the ambiguity associated with the different approaches undoubtedly affects the driving forces and, thus, the evolution of the grain boundaries. Consequently, artifacts regarding the plastic material behavior would lead to an artificial or even non-physical evolution of the underlying microstructure.

1.5 Objective of the current work

The main objective of the work at hand is the discussion of the implementation of the CP within the diffuse interface through different approaches and associated consequences, such as unphysical artifacts of the plastic material behavior present for the interpolation approach. It is illustrated that the jump condition approach is a suitable approach for the computation of the plastic material behavior within the diffuse interface region. To this end, the classical CP theory is implemented within the multiphase-field method by means of the jump condition approach. This implementation, referred to as phase-specific plastic field approach (PSPFA), is discussed in detail and illustrated by a schematic flowchart. A comparison between the PSPFA and a possible implementation by means of the interpolation approach, denoted as common plastic fields approach (CPFA), is carried out with respect to a three dimensional bicrystal simulation. This allows for an illustrative discussion of the artifacts inherent to the CPFA that are already present within the diffuse interface between two phases. To this end, the solution of a sharp-interface simulation is compared to the results obtained by the PSPFA and to a set-up mimicking the CPFA. Thereby, artifacts intrinsic to the CPFA are discussed and highlighted. The application of the implementation of the CP theory in terms of the PSPFA to more complex microstructures is demonstrated by simulations regarding a periodic honeycomb structure as well as a grain aggregate consisting of eight differently oriented grains, denoted as octotuple. While the different approaches would clearly affect the evolution of an underlying oligo- or polycrystalline microstrucutre, no evolving microstructure is considered in this work, for brevity. This discussion would go beyond the scope of this work and is of future consider-

ations. A discussion regarding the effect of the variation of the interface width on the strain obtained by the CPFA and the PSPFA is provided. In this context, the distributions of selected strain components are discussed with respect to the longitudinal axis of the bicrystal.

1.6 Originality

A new multiphase-field approach to small strain crystal plasticity is presented. In contrast to existing approaches, the approach presented accounts for the balance equations on singular surfaces as well as for phase-specific plastic fields, and does not consider an interpolation of crystallographic orientations of adjacent grains. Here, a bicrystal is used as an illustrative trivial form to compare the results obtained with the new approach, the interpolation approach, and the sharp interface solution. The results obtained with the newly presented approach are in good agreement with the results from the sharp interface theory, while the interpolation approach yields significant deviations from the sharp interface in and out of the diffuse interface.

1.7 Outline

In Sect. 2, the preliminaries of the CP theory and the considered MPFM are briefly revisited. The implementation of the CP theory regarding bulk material and the diffuse interface region is discussed in detail in Sect. 3. Section 4 provides the illustration of the considererd BVPs as well as the discussion of the results. The manuscript is concluded in Sect. 5.

1.8 Notation

In this work, a direct tensor notation is used. Scalars, vectors, tensors of second and of fourth order are written as a, $\boldsymbol{a}$, $\boldsymbol{A}$, and $\mathbb{A}$, respectively. Regarding two tensors, each of first, second or fourth order, the scalar product is written as $\boldsymbol{a}\cdot\boldsymbol{b}$, $\boldsymbol{A}\cdot\boldsymbol{B}$, and $\mathbb{A}\cdot\mathbb{B}$. Moreover, $\boldsymbol{A}\boldsymbol{b}$ and $\mathbb{A}[\boldsymbol{B}]$ denote the linear mapping of a vector by a tensor of 2nd order and the mapping of a 2nd order tensor by a 4th order tensor, respectively. Between two tensors of 2nd or 4th order the composition is written as $\boldsymbol{A}\boldsymbol{B}$ or $\mathbb{A}\mathbb{B}$. In addition, $\dot{a}$ denotes the material time derivative of field a of arbitrary tensorial order.

2 Modeling and theoretical preliminaries of crystal plasticity

2.1 Balance equations of a Cauchy continuum and constitutive modeling

2.1.1 Energy balance

In this section, a material volume, is considered, divided by a material singular surface $\mathcal{S}$ into the subvolumes $\mathcal{V}^+$ and $\mathcal{V}^-$. Against the surrounding, the volumes $\mathcal{V}^+$ and $\mathcal{V}^-$ are bounded by $\mathcal{F}^+$ and $\mathcal{F}^-$. Regarding $\mathcal{S}$, the corresponding normal vector $\boldsymbol{n}_{\mathcal{S}}$ points from $\mathcal{V}^-$ to $\mathcal{V}^+$. The outer normal vectors on $\mathcal{F}^+$ and $\mathcal{F}^-$ are denoted as $\boldsymbol{n}_{\mathcal{V}}^+$ and $\boldsymbol{n}_{\mathcal{V}}^-$, respectively. The relation $\boldsymbol{n}_{\mathcal{S}} = \boldsymbol{n}_{\mathcal{V}}^+ = -\boldsymbol{n}_{\mathcal{V}}^-$ holds due to the pill-box theorem, cf., e.g., [58]. Across $\mathcal{S}$, the jump of an arbitrary quantity π is denoted as $\{\pi\} = \pi^+ - \pi^-$, with the corresponding limit value π^+ and π^- from $\mathcal{V}^+$ and $\mathcal{V}^-$, respectively. Subsequently, the velocity fields of the material volume and of the singular surface are referred to as $\boldsymbol{v}$ and $\boldsymbol{v}^{\mathcal{S}}$, respectively. Here, grain boundaries are modeled by material singular surfaces for which $\boldsymbol{v} = \boldsymbol{v}^{\mathcal{S}}$ and $\{\boldsymbol{v}\} = \boldsymbol{0}$ hold true, cf., e.g., [59, pp. 345, 346]. With respect to the current configuration, the balance of total energy for the above described continuum is given by

$$\frac{\mathrm{d}}{\mathrm{d}t}\int\limits_{\mathcal{V}^+\cup\mathcal{V}^-}\rho\left(e+\frac{1}{2}\boldsymbol{v}\cdot\boldsymbol{v}\right)\mathrm{d}v = \int\limits_{\mathcal{V}^+\cup\mathcal{V}^-}\rho\,(\boldsymbol{b}\cdot\boldsymbol{v}+r)\,\mathrm{d}v + \int\limits_{\mathcal{F}^+\cup\mathcal{F}^-}(\boldsymbol{t}\cdot\boldsymbol{v}+h)\,\mathrm{d}a, \tag{1}$$

cf., e.g., [58, pp. 57–60], [20]. In this context, the mass density is referred to as ρ, the specific internal energy as e, the body force as $\boldsymbol{b}$, the heat supply as r, the traction force as $\boldsymbol{t}$, and the heat flux as h. Regarding the singular surface, no contributions are considered additionally. Therefore, no integrals with respect to $\mathcal{S}$ are considered in Eq. (1) in contrast to, e.g., [20, Eq. (1)].

2.1.2 Balance equations

Regarding a continuum without a singular surface, of volume $\mathcal{V}_t$, the existence of the heat flux vector $\boldsymbol{q}$ and the Cauchy stress tensor $\boldsymbol{\sigma}$ via the relations $h = -\boldsymbol{q}\cdot\boldsymbol{n}_{\mathcal{V}}$ and $\boldsymbol{t} = \boldsymbol{\sigma}\boldsymbol{n}_{\mathcal{V}}$ as well as the balance equations in regular points are obtained by invariance of the balance of total energy with respect to a change of observer, cf., e.g., [60]. In this context, $\boldsymbol{n}_{\mathcal{V}}$ denotes the outer normal vector on $\partial\mathcal{V}_t$. For a continuum containing a material singular surface, the derivation of the balance equations at the singular surface by means of invariance considerations is discussed, e.g., by [20]. With respect to Eq. (1), the balance of mass, linear, and angular momentum for regular points read

$$\dot{\rho} + \rho\,\mathrm{div}\,(\boldsymbol{v}) = 0, \quad \rho\,(\boldsymbol{a}-\boldsymbol{b}) = \mathrm{div}\,(\boldsymbol{\sigma}), \quad \boldsymbol{\sigma} = \boldsymbol{\sigma}^{\mathsf{T}}. \tag{2}$$

Moreover, the balance of internal energy is obtained as $\rho\dot{e} = \boldsymbol{\sigma}\cdot\boldsymbol{D} + \rho r - \mathrm{div}\,(\boldsymbol{q})$, with the acceleration $\boldsymbol{a} = \dot{\boldsymbol{v}}$ and $\boldsymbol{D}$ as the symmetric part of the velocity gradient. For singular points only the balance of linear momentum

$$\{\boldsymbol{t}\} = \boldsymbol{0} \tag{3}$$

and internal energy, i.e., $\{\boldsymbol{q}\} \cdot \boldsymbol{n}_{\mathcal{S}} = \boldsymbol{0}$, remain non-vanishing. The balance of linear momentum according to Eq. (3) and the Hadamard condition, introduced later, are considered to hold true in each point within the diffuse interface, in the context of the jump condition approach. Subsequently, the following assumptions are made

A1 Considerations are limited to a small strain theory, thereby, implying a constant mass density, cf. [61, p. 31]. Moreover, $\boldsymbol{D} = \dot{\boldsymbol{\varepsilon}}$ as well as $(\dot{\ }) = \partial/\partial t$ holds true, with $\dot{\boldsymbol{\varepsilon}}$ as the rate of the infinitesimal strain tensor, cf. [61, p. 32].
A2 Body forces are neglected, i.e., $\boldsymbol{b} = \boldsymbol{0}$.
A3 The quasi-static special case is considered, i.e., $\boldsymbol{a} = \boldsymbol{0}$ holds true.

2.1.3 Constitutive material behavior regarding bulk

In the work at hand, a thermodynamically consistent crystal plasticity theory is considered. The corresponding constitutive equations are briefly commented and stated in Table 1. Regarding bulk material, the related assumptions are discussed, e.g., by [62, A. 1-3 & A6-11].

The additive decomposition of the infinitesimal strain tensor, i.e., $\boldsymbol{\varepsilon} = \boldsymbol{\varepsilon}^{\mathrm{e}} + \boldsymbol{\varepsilon}^{\mathrm{p}}$ into the elastic strain $\boldsymbol{\varepsilon}^{\mathrm{e}}$ and the plastic strain $\boldsymbol{\varepsilon}^{\mathrm{p}}$ is accounted for by Hooke's law, with $\mathbb{C}$ denoting the stiffness tensor. The plastic strain is assumed to account for the plastic slips γ_ξ, the slip plane normal $\boldsymbol{n}_\xi$, and the slip direction $\boldsymbol{d}_\xi$ of each slip system, cf., e.g., [63] regarding the slip systems of an FCC crystal. In this context, $\boldsymbol{M}_\xi$ is referred to as the Schmid tensor of slip system ξ. For each slip system, the evolution of the plastic slip is described by an evolution equation in form of an ordinary differential equation, representing a viscous flow rule, cf., e.g., [64–66], of overstress type, cf., e.g., [67, Eq. (1.16)], [68, Eq. (1.24)]. The viscous flow rule, also referred to as rate-dependent flow rule, represents an approximation of the rate-independent theory, cf., e.g., [67, p. 30], [69, p. 601], if large values of the sensitivity exponent $m > 0$ are considered, cf., e.g., [35, p. 42]. Regarding plastic slip occurring on multiple slip systems, the determination of the plastic slip can lead to problems, as discussed by [70, pp. 278 & 284]. Here, $\dot{\gamma}_0$ denotes the referential shear rate, τ_ξ the resolved shear stress, τ_{C} the critical shear stress, $\tau_{\mathrm{D}} > 0$ the drag stress, and $m > 0$ the sensitivity exponent. Moreover, regarding an arbitrary quantity a, the Macaulay brackets are defined as $\langle a \rangle = (a + |a|)/2$. Consequently, the sign of $\dot{\gamma}_\xi$ and τ_ξ coincide. It is assumed that the critical shear stress is associated with an isotropic Voce hardening, with the initial yield stress τ_0, the saturation stress τ_∞, the initial hardening modulus Θ_0, and the accumulated plastic slip γ_{ac} defined by $\dot{\gamma}_{\mathrm{ac}} = \sum_{\alpha=1}^{N} |\dot{\gamma}_\xi|$. Here, N denotes the number of active slip systems.

2.2 Crystal plasticity in the context of the multiphase-field method

2.2.1 Free energy functional

In the work at hand, the governing equations of the multiphase-field method (MPFM), cf., e.g., [71–73], originate from the subsequently stated free energy functional $\mathcal{F}$, reading

$$\mathcal{F}[\boldsymbol{\phi}, \nabla\boldsymbol{\phi}, \boldsymbol{u}] = \int_{\mathcal{V}} f \,\mathrm{d}v = \int_{\mathcal{V}} f_{\mathrm{grad}} + f_{\mathrm{pot}} + \overline{f}_{\mathrm{bulk}} \,\mathrm{d}v. \tag{4}$$

Here, the free energy density f is additively decomposed into the contributions f_{grad}, f_{pot}, and $\overline{f}_{\mathrm{bulk}}$. They depend, among others, on the order parameters which are briefly noted in terms of the n-tuple $\boldsymbol{\phi} = \{\phi_1, \ldots, \phi_{N^*}\}$. In this context, N^* refers to the number of phases in the sense of subregions of different ordering state. Interpreting the order parameters as volume fractions of the corresponding phase, they have to fulfill the summation constraint

$$\sum_{\alpha=1}^{N^*} \phi_\alpha(\boldsymbol{x}, t) = 1, \quad \forall \boldsymbol{x} \in \mathcal{V}, t \geq 0. \tag{5}$$

For brevity, no evolution of the underlying crystalline microstructure is considered in the present work. Thus, the contributions f_{grad} and f_{pot}, related to the regularization of an SI towards a diffuse interface, are not discussed here, but provided in the "Appendix", along with the evolution equation of the order parameter, cf. Eq. (A15), and the considered driving forces, cf. Eqs. (A12)–(A14). The contribution $\overline{f}_{\mathrm{bulk}}$ accounts for the considered material behavior and is additively decomposed into an elastic contribution $\overline{f}_{\mathrm{e}}$ and a plastic contribution $\overline{f}_{\mathrm{p}}$. Consequently,

$$\overline{f}_{\mathrm{bulk}} = \overline{f}_{\mathrm{e}} + \overline{f}_{\mathrm{p}} \tag{6}$$

holds true. Regarding the plastic contribution $\overline{f}_{\mathrm{p}}$ two approaches are discussed by [74] which are revisited in the following. Before introducing the contributions $\overline{f}_{\mathrm{e}}$ and $\overline{f}_{\mathrm{p}}$ in detail, some kinematic relations are to be discussed.

2.2.2 Kinematical relations used subsequently

Within the context of the MPFM, the jump of an arbitrary quantity π is commonly given with respect to the corresponding phases. Subsequently, $\{\pi\}^{\alpha\beta} = \pi^\alpha - \pi^\beta$ is considered, with respect to the adjacent phases α and β, instead of $\{\pi\} = \pi^+ - \pi^-$. For the computation of phase-specific

Table 1 Summary of CP theory

Additive decomposition	$\boldsymbol{\varepsilon} = \boldsymbol{\varepsilon}^{\mathrm{e}} + \boldsymbol{\varepsilon}^{\mathrm{p}}$
Hooke's law	$\boldsymbol{\sigma} = \mathbb{C}\left[\boldsymbol{\varepsilon} - \boldsymbol{\varepsilon}^{\mathrm{p}}\right]$
Plastic strain	$\boldsymbol{\varepsilon}^{\mathrm{p}} = \sum_{\xi=1}^{N} \gamma_\xi \, \boldsymbol{M}_\xi, \quad \boldsymbol{M}_\xi = \mathrm{sym}\left(\boldsymbol{n}_\xi \otimes \boldsymbol{d}_\xi\right)$
Flow rule	$\dot{\gamma}_\xi = \dot{\gamma}_0 \left\langle \frac{\lvert\tau_\xi\rvert - \tau_{\mathrm{C}}}{\tau_{\mathrm{D}}} \right\rangle^m \mathrm{sgn}\left(\tau_\xi\right), \quad \tau_\xi = \boldsymbol{\sigma} \cdot \boldsymbol{M}_\xi$
Critical shear stress	$\tau_{\mathrm{C}}(\gamma_{\mathrm{ac}}) = \tau_\infty - (\tau_\infty - \tau_0) \exp\left(\frac{-\Theta_0}{\tau_\infty - \tau_0} \gamma_{\mathrm{ac}}\right)$
Accumulated plastic slip	$\dot{\gamma}_{\mathrm{ac}} = \sum_{\xi=1}^{N} \lvert\dot{\gamma}_\xi\rvert$

The considered constitutive material behavior consists of the additive decomposition of the infinitesimal strain tensor, Hooke's law, the assumption for the plastic strain tensor, the flow rules for each plastic slip, the definition of the critical shear stress, and the accumulated plastic strain, as well as the yield criterion evaluated at each slip system

strains, the balance of linear momentum at a material singular surface, cf. Eq. (3), as well as the Hadamard condition, i.e., the kinematic jump condition regarding the deformation gradient $\boldsymbol{F}$, are considered, cf., e.g., [75, Eq. $(2.2.9)_1$]. Taking into account the relation between the deformation gradient and the displacement gradient $\boldsymbol{H} = \mathrm{grad}\,(\boldsymbol{u})$, with $\boldsymbol{u}$ denoting the displacement field, i.e., $\boldsymbol{H} = \boldsymbol{F} - \boldsymbol{I}$, the jump condition for the displacement gradient is given by

$$\{\boldsymbol{H}\}^{\alpha\beta} = \boldsymbol{a}^{\alpha\beta} \otimes \boldsymbol{n}^{\alpha\beta}, \quad \text{with } \{\boldsymbol{H}\}^{\alpha\beta} = \boldsymbol{H}^{\alpha} - \boldsymbol{H}^{\beta}. \tag{7}$$

In this context, $\boldsymbol{a}^{\alpha\beta}$ denotes the unknown jump vector and $\boldsymbol{n}^{\alpha\beta}$ the normal vector from phase α to phase β. Within the diffuse interface, the displacement gradient $\boldsymbol{H}$ is assumed to be given by the interpolation of the phase-specific displacement gradients, reading

$$\boldsymbol{H} = \sum_{\alpha=1}^{N^*} \phi_\alpha \boldsymbol{H}^{\alpha}, \tag{8}$$

cf., e.g., [54, p. 207] in the context of large deformations. From Eq. (7) it follows that

$$\{\boldsymbol{H}\}^{\alpha\beta} = \boldsymbol{H}^{\alpha} - \boldsymbol{H}^{\beta} = -(\boldsymbol{H}^{\beta} - \boldsymbol{H}^{\alpha}) = -\{\boldsymbol{H}\}^{\beta\alpha}. \tag{9}$$

Accounting for the combination of Eqs. (7), (8), and (9), the phase-specific displacement gradient can be expressed in terms of the interpolated displacement gradient and the jumps of the displacement gradients as

$$\boldsymbol{H}^{\beta} = \boldsymbol{H} - \sum_{\delta=1,\delta\neq\beta}^{N^*} \phi_\delta \{\boldsymbol{H}\}^{\delta\beta}, \quad \boldsymbol{H}^{\beta} = \boldsymbol{H} + \sum_{\delta=1,\delta\neq\beta}^{N^*} \phi_\delta \{\boldsymbol{H}\}^{\beta\delta} \tag{10}$$

cf., e.g., [74, Eq. (7)]. Introducing $\boldsymbol{\varepsilon} = \mathrm{sym}\,(\boldsymbol{H})$, and accounting for Eq. $(10)_2$ the phase-specific strains can also be expressed in terms of $\boldsymbol{\varepsilon}$ and the jumps $\{\boldsymbol{\varepsilon}\}^{\beta\delta}$, reading

$$\boldsymbol{\varepsilon}^{\beta} = \boldsymbol{\varepsilon} + \sum_{\delta=1,\delta\neq\beta}^{N^*} \phi_\delta \{\boldsymbol{\varepsilon}\}^{\beta\delta}. \tag{11}$$

2.2.3 Elastic free energy density

The elastic contribution $\overline{f}_{\mathrm{e}}$ is given by the interpolation of the phase-specific elastic free energy densities, i.e.,

$$\overline{f}_{\mathrm{e}} = \sum_{\alpha=1}^{N^*} \phi_\alpha f_{\mathrm{e},\alpha}. \tag{12}$$

For each phase, the elastic free energy density is formulated in terms of the phase-specific strains and the phase-specific plastic strains, reading

$$f_{\mathrm{e},\alpha}(\boldsymbol{\varepsilon}^{\alpha}(\boldsymbol{\phi}) - \boldsymbol{\varepsilon}^{\mathrm{p},\alpha}) = \frac{1}{2}\left(\boldsymbol{\varepsilon}^{\alpha}(\boldsymbol{\phi}) - \boldsymbol{\varepsilon}^{\mathrm{p},\alpha}\right) \cdot \left(\mathbb{C}^{\alpha}\left[\boldsymbol{\varepsilon}^{\alpha}(\boldsymbol{\phi}) - \boldsymbol{\varepsilon}^{\mathrm{p},\alpha}\right]\right), \tag{13}$$

cf., e.g., [74, p. 1402]. Here, the phase-specific stiffness tensor is referred to as $\mathbb{C}^{\alpha}$. Due to Eq. (11), the phase-specific strains depend on the order parameters, while the phase-specific plastic strains are independent of the order parameters. The minimization of Eq. (4) with respect to the displacement field $\boldsymbol{u}$ yields the balance of linear momentum within the diffuse interface region, reading

$$\mathrm{div}\,(\overline{\boldsymbol{\sigma}}) = \boldsymbol{0}, \quad \overline{\boldsymbol{\sigma}} = \sum_{\alpha=1}^{N^*} \phi_\alpha \boldsymbol{\sigma}^{\alpha}, \tag{14}$$

with the interpolated stress tensor $\overline{\boldsymbol{\sigma}}$, cf., e.g., [54, Eq. (9)] in the context of large deformations.

2.2.4 Remark on approaches of implementing plasticity in a diffuse interface

Regarding the implementation of a plasticity theory within a diffuse interface, the interpolation approach is compared with the jump condition approach by [74]. In the work at hand, the interpolation approach, associated with a shared plasticity field, is referred to as common plastic fields approach (CPFA) while the jump condition approach, based on phase-inherent plastic fields, is referred to as phase-specific plastic fields approach (PSPFA). In [74], the drawbacks of the CPFA and the advantages of the PSPFA are discussed in the context of Mises plasticity with respect to a tensile test: The CPFA yields unphysical results if a high contrast regarding the yield stress of adjacent phases is considered. Here, this result is further strengthened with respect to crystal plasticity. For an appropriate discussion, both the CPFA and the PSPFA are briefly reviewed in the context of Voce hardening. Clearly, neither the CPFA nor the PSPFA are limited to a specific hardening behavior. Finally, it is emphasized that the PSPFA is favorable compared to the CPFA regarding crystal plasticity as well. The implementation of the CP in the context of the MPFM is motivated by the need of tracking grain boundaries in an evolving, polycrystalline microstructure due to solid-solid phase transformations, leading to an evolution and migration of all grain boundaries. As the evolution of the grain boundaries is, among others, affected by the computed plastic fields, artifacts due to a chosen implementation of the CP would inevitably lead to artifacts of the evolution of the grain boundaries. Consequently, the implementation of the crystal plasticity theory is not carried out and discussed within the CPFA, but only within the PSPFA.

2.2.5 Common plastic fields approach

The CPFA accounts for interpolated material parameters, such as the interpolated initial yield stress $\overline{\tau}_0$, the interpolated saturation stress $\overline{\tau}_\infty$, and the interpolated initial hardening modulus $\overline{\Theta}_0$, given by

$$\overline{\tau}_0 = \sum_{\alpha=1}^{N^*} \phi_\alpha \tau_0^\alpha, \quad \overline{\tau}_\infty = \sum_{\alpha=1}^{N^*} \phi_\alpha \tau_\infty^\alpha, \quad \overline{\Theta}_0 = \sum_{\alpha=1}^{N^*} \phi_\alpha \Theta_0^\alpha, \tag{15}$$

cf., e.g., [76, Eqs. (10)–(12)]. With the interpolated material parameters, one plastic contribution is formulated in terms of the accumulated plastic slip γ_{ac} within the interface, reading

$$\overline{f}_{\mathrm{p}} = \left((\overline{\tau}_\infty - \overline{\tau}_0)\, \gamma_{\mathrm{ac}} + \frac{(\overline{\tau}_\infty - \overline{\tau}_0)^2}{\overline{\Theta}_0} \exp\left(\frac{-\overline{\Theta}_0}{\overline{\tau}_\infty - \overline{\tau}_0} \gamma_{\mathrm{ac}} \right) \right). \tag{16}$$

Consequently, within the diffuse interface region, only one accumulated plastic slip is considered. In contrast to Mises plasticity, the crystallographic orientation is accounted for by crystal plasticity. Thus, given two adjacent phases with different lattice orientation, the lattice orientation within the diffuse interface is then obtained as an interpolation between both orientations, regarding the CPFA, cf., e.g., [77, Fig. 1 (b)]. By this, compared to the SI problem, artificial intermediate-orientations are introduced within the diffuse interface region in the context of the CPFA. The associated consequences are discussed in the subsequent section.

2.2.6 Phase-specific-plastic fields approach

Regarding the PSPFA, the plastic free energy densities of each phase are interpolated as done for with the elastic free energy densities, leading to

$$\overline{f}_{\mathrm{p}} = \sum_{\alpha=1}^{N^*} \phi_\alpha f_{\mathrm{p},\alpha}(\gamma_{\mathrm{ac}}^\alpha). \tag{17}$$

For each phase, its own material parameters are considered and, thus, each phase is represented by its respective free energy density within the diffuse interface region, reading

$$f_{\mathrm{p},\alpha}(\gamma_{\mathrm{ac}}^\alpha) = (\tau_\infty^\alpha - \tau_0^\alpha)\, \gamma_{\mathrm{ac}}^\alpha + \frac{(\tau_\infty^\alpha - \tau_0^\alpha)^2}{\Theta_0} \exp\left(\frac{-\Theta_0^\alpha}{\tau_\infty^\alpha - \tau_0^\alpha} \gamma_{\mathrm{ac}}^\alpha \right). \tag{18}$$

Moreover, each phase is represented with its specific orientation, that is also present in the bulk region, within the diffuse interface region. Consequently, no artificial intermediate orientations are introduced in the diffuse interface.

3 Numerical implementation of classical crystal plasticity

3.1 Global problem regarding one phase

3.1.1 Weak form of the balance of linear momentum

In the work at hand, the Finite Element Method (FEM) is used to solve the balance of linear momentum and to account for crystal plasticity, involving a weak form of the balance of linear momentum given by

$$\mathcal{G}[\boldsymbol{u}] = \int_{\mathcal{V}_t} \mathrm{grad}\,(\boldsymbol{f}) \cdot \boldsymbol{\sigma}(\boldsymbol{u})\, \mathrm{d}v - \int_{\partial \mathcal{V}_t} \boldsymbol{t} \cdot \boldsymbol{f}\, \mathrm{d}a = 0, \tag{19}$$

where $\boldsymbol{f}$ is a vectorial test function. The weak form of the balance of linear momentum according to Eq. (19) is briefly referred to as *weak form*, subsequently. Considering a highly

nonlinear material behavior, an iterative solution scheme is applied and, thereby, a linearization of the weak form, cf., e.g., [78, p. 174]. To this end, a time-discretized, cf., e.g., [79, pp. 6–9], so called incremental formulation, cf., e.g., [80], of the weak form is considered.

3.1.2 Incremental formulation

Regarding a time-step t_{n} and $\boldsymbol{u}_{\mathrm{n}} = \boldsymbol{u}(t_{\mathrm{n}})$, the time-discretized weak form is briefly denoted as $\mathcal{G}[\boldsymbol{u}_{\mathrm{n}}]$. At t_{n}, the values of the infinitesimal strain $\boldsymbol{\varepsilon}_{\mathrm{n}} = \boldsymbol{\varepsilon}(t_{\mathrm{n}})$, the plastic strain $\boldsymbol{\varepsilon}^{\mathrm{p}}_{\mathrm{n}} = \boldsymbol{\varepsilon}^{\mathrm{p}}(t_{\mathrm{n}})$, the Cauchy stress $\boldsymbol{\sigma}_{\mathrm{n}} = \boldsymbol{\sigma}(t_{\mathrm{n}})$, and the accumulated plastic slip $\gamma_{\mathrm{ac,n}} = \gamma_{\mathrm{ac}}(t_{\mathrm{n}})$ are known. The linearization of the time-discretized weak form, cf., e.g., [81, Eq. (2.1)], is commonly combined with a (quasi) Newton method as iterative solution scheme for the computation of the unknown fields with respect to the time-step $t_{\mathrm{n+1}}$, cf., e.g., [79, Eqs. (1.28)–(1.35)]. In this context, several iterations of the applied (quasi) Newton method are performed. While the subscripts n and $n+1$ are associated with the corresponding time step, the superscripts i and $i+1$ are associated with the iterations, as introduced by [80, p. 106, remark 3.1 and 3.2], and the linearized form can be denoted as $\mathcal{G}[\boldsymbol{u}^{i}_{\mathrm{n+1}}] + \mathcal{D}_{\mathrm{u}}\left\{\mathcal{G}[\boldsymbol{u}^{i}_{\mathrm{n+1}}]\right\} \cdot \Delta\boldsymbol{u}^{i}_{\mathrm{n+1}} \approx 0$. The convergence of the Newton method yields the fields at $t_{\mathrm{n+1}}$. The solution procedure of the time-discretized weak form is referred to as the *global solver*, in the following.

3.2 Local problem—crystal plasticity regarding one phase

3.2.1 Implicit integration

Regarding the ith iteration, at each integration point, the computation of the values $\boldsymbol{\varepsilon}^{\mathrm{p,i}}_{\mathrm{n+1}}$, $\boldsymbol{\sigma}^{i}_{\mathrm{n+1}}$, and $\gamma^{i}_{\mathrm{ac,n+1}}$ is based solely on the known values of $\boldsymbol{\varepsilon}_{\mathrm{n}}$, $\boldsymbol{\varepsilon}^{\mathrm{p}}_{\mathrm{n}}$, and $\gamma_{\mathrm{ac,n}}$ of the previously converged Newton-iteration at t_{n}, as well as the strain- and time increments $\Delta\boldsymbol{\varepsilon}$, Δt, cf., e.g., [80, Sect. 3]. Regarding the applied algorithm, $\boldsymbol{\varepsilon}^{\mathrm{p,i}}_{\mathrm{n+1}}$ and $\gamma^{i}_{\mathrm{ac,n+1}}$ are determined based on the rate formulation of the plastic strain and the definition of the accumulated plastic slip, both stated in Table 1, by means of the backward (implicit) Euler, cf. [78, p. 33]. Since this procedure is considered with respect to a specific iteration, the superscript i, indicating the iteration, is dropped for a better readability, subsequently. In the context of small deformations, the slip plane normals and slip directions are assumed to be constant with respect to time. Thus, application of the backward Euler to the rate-form of the plastic strain yields

$$\frac{\boldsymbol{\varepsilon}^{\mathrm{p}}_{\mathrm{n+1}} - \boldsymbol{\varepsilon}^{\mathrm{p}}_{\mathrm{n}}}{\Delta t} \approx \dot{\gamma}_0 \sum_{\xi=1}^{N} \left\langle \frac{\left|\tau_\xi(\boldsymbol{\varepsilon}_{\mathrm{n+1}}, \boldsymbol{\varepsilon}^{\mathrm{p}}_{\mathrm{n+1}})\right| - \tau_{\mathrm{C}}(\gamma_{\mathrm{ac,n+1}})}{\tau_{\mathrm{D}}} \right\rangle^{m} \operatorname{sgn}\left(\tau^{n+1}_{\xi}\right) \boldsymbol{M}_{\xi}. \tag{20}$$

Application of the backward Euler to the definition of the plastic slip yields

$$\frac{\gamma_{\mathrm{ac,n+1}} - \gamma_{\mathrm{ac,n}}}{\Delta t} \approx \dot{\gamma}_0 \sum_{\xi=1}^{N} \left\langle \frac{\left|\tau_\xi(\boldsymbol{\varepsilon}_{\mathrm{n+1}}, \boldsymbol{\varepsilon}^{\mathrm{p}}_{\mathrm{n+1}})\right| - \tau_{\mathrm{C}}(\gamma_{\mathrm{ac,n+1}})}{\tau_{\mathrm{D}}} \right\rangle^{m}. \tag{21}$$

3.2.2 Newton procedure

Equations (20) and (21) constitute a system of coupled nonlinear equations regarding the unknowns $\boldsymbol{\varepsilon}^{\mathrm{p}}_{\mathrm{n+1}}$ and $\gamma_{\mathrm{ac,n+1}}$. In the work at hand, it is solved by means of a Newton procedure. In this context, the following residuals are defined

$$\boldsymbol{g}_1 := \boldsymbol{\varepsilon}^{\mathrm{p}}_{\mathrm{n+1}} - \boldsymbol{\varepsilon}^{\mathrm{p}}_{\mathrm{n}} - \Delta t\,\dot{\gamma}_0 \sum_{\xi=1}^{N} \left\langle \frac{\left|\tau^{n+1}_{\xi}\right| - \tau^{n+1}_{\mathrm{C}}}{\tau_{\mathrm{D}}} \right\rangle^{m} \operatorname{sgn}\left(\tau^{n+1}_{\xi}\right) \boldsymbol{M}_{\xi} = \boldsymbol{0} \tag{22}$$

$$g_2 := \gamma_{\mathrm{ac,n+1}} - \gamma_{\mathrm{ac,n}} - \Delta t\,\dot{\gamma}_0 \sum_{\xi=1}^{N} \left\langle \frac{\left|\tau^{n+1}_{\xi}\right| - \tau^{n+1}_{\mathrm{C}}}{\tau_{\mathrm{D}}} \right\rangle^{m} = 0, \tag{23}$$

where $\tau^{n+1}_{\xi} := \tau_\xi(\boldsymbol{\varepsilon}_{\mathrm{n+1}}, \boldsymbol{\varepsilon}^{\mathrm{p}}_{\mathrm{n+1}})$ and $\tau^{n+1}_{\mathrm{C}} := \tau_{\mathrm{C}}(\gamma_{\mathrm{ac,n+1}})$ are introduced. Regarding this so-called *local* Newton procedure, the partial derivatives of Eq. (22) and Eq. (23) with respect to $\boldsymbol{\varepsilon}^{\mathrm{p}}_{\mathrm{n+1}}$ and $\gamma_{\mathrm{ac,n+1}}$ are required. They are summarized by the Box illustrated in Fig. 1.

3.3 Local problem—crystal plasticity regarding diffuse interface region

3.3.1 Computation of phase-specific strains

For a better readability, the equations regarding the diffuse interface region are formulated with respect to two phases α and β, subsequently. Clearly, the treatment of CP theory is not limited to two phases, but is directly applicable to multiple phases, as illustrated by the simulation of a periodic honeycomb structure and an octotuple. The global solver computes the overall displacement field and, thus, provides the strain $\boldsymbol{\varepsilon}_{\mathrm{n+1}}$. However, regarding a diffuse interface region between two phases α and β, the solution of the local problem requires the phase-specific strains $\boldsymbol{\varepsilon}^{\alpha}_{\mathrm{n+1}}$ and $\boldsymbol{\varepsilon}^{\beta}_{\mathrm{n+1}}$. To this

$$\frac{\partial \boldsymbol{g}_1}{\partial \boldsymbol{\varepsilon}^{\mathrm{p}}_{\mathrm{n+1}}} = \mathbb{I}^{\mathrm{S}}_{\langle 4\rangle} + \frac{\Delta t \dot{\gamma}_0 m}{\tau_{\mathrm{D}}} \sum_{\xi=1}^{N} \tilde{\tau}_\xi \left(\mathbb{C}\mathbb{M}_{\langle 4\rangle}\right)^{\mathsf{T}_{\mathsf{H}}}, \qquad \mathbb{M}_{\langle 4\rangle} = \boldsymbol{M}_\xi \otimes \boldsymbol{M}_\xi,$$

$$\frac{\partial \boldsymbol{g}_1}{\partial \gamma_{\mathrm{ac,n+1}}} = \frac{\Delta t \dot{\gamma}_0 m}{\tau_{\mathrm{D}}} \frac{\partial \tau_{\mathrm{C}}}{\partial \gamma_{\mathrm{ac,n+1}}} \sum_{\xi=1}^{N} \tilde{\tau}_\xi \ \mathrm{sgn}\left(\tau_\xi^{n+1}\right) \boldsymbol{M}_\xi, \qquad \tilde{\tau}_\xi = \left\langle \frac{\left|\tau_\xi^{n+1}\right| - \tau_{\mathrm{C}}^{n+1}}{\tau_{\mathrm{D}}} \right\rangle^{m-1},$$

$$\frac{\partial g_2}{\partial \boldsymbol{\varepsilon}^{\mathrm{p}}_{\mathrm{n+1}}} = \frac{\Delta t \dot{\gamma}_0 m}{\tau_{\mathrm{D}}} \sum_{\xi=1}^{N} \tilde{\tau}_\xi \ \mathrm{sgn}\left(\tau_\xi^{n+1}\right) \mathbb{C}\left[\boldsymbol{M}_\xi\right], \qquad \frac{\partial \tau_{\mathrm{C}}}{\partial \gamma_{\mathrm{ac,n+1}}} = \Theta_0 \exp\left(\frac{-\Theta_0 \gamma_{\mathrm{ac,n+1}}}{\tau_\infty - \tau_0}\right),$$

$$\frac{\partial g_2}{\partial \gamma_{\mathrm{ac,n+1}}} = 1 + \frac{\Delta t \dot{\gamma}_0 m}{\tau_{\mathrm{D}}} \frac{\partial \tau_{\mathrm{C}}}{\partial \gamma_{\mathrm{ac,n+1}}} \sum_{\xi=1}^{N} \tilde{\tau}_\xi.$$

Fig. 1 Derivatives of residuals, involved in the solution of the local problem. Here, $\mathbb{I}^{\mathrm{S}}_{\langle 4\rangle}$ denotes the symmetric identity of fourth order, cf. , e.g., [82, Eq. (1.29)] and $\mathbb{C}$ the stiffness tensor of fourth order. Moreover, the abbreviations $\mathbb{M}_{\langle 4\rangle}$ and $\tilde{\tau}_\xi$ as well as the derivative $\partial \tau_{\mathrm{C}} / \partial \gamma_{\mathrm{ac,n+1}}$ are given

end, the jump-condition approach is applied, which is discussed in detail by [54] in the context of large deformations and applied, e.g., by [74] with respect to Mises plasticity or [83] regarding visco-elasticity. The jump condition approach accounts for the fulfillment of the balance of linear momentum at a singular surface, cf. Eq. (3), as well as the Hadamard condition, cf. Eq. (7), at each point within the diffuse interface region. Regarding two phases, for brevity, Eq. (3) reads

$$\begin{aligned} \boldsymbol{g}^{\alpha\beta} = &\left(\mathbb{C}^\alpha \left[\boldsymbol{\varepsilon}^\alpha_{\mathrm{n+1}}\left(\boldsymbol{a}^{\alpha\beta}_{\mathrm{n+1}}\right) - \boldsymbol{\varepsilon}^{\mathrm{p},\alpha}_{\mathrm{n+1}}\right]\right. \\ &\left. - \mathbb{C}^\beta \left[\boldsymbol{\varepsilon}^{\alpha B}_{\mathrm{n+1}}\left(\boldsymbol{a}^{\alpha\beta}_{\mathrm{n+1}}\right) - \boldsymbol{\varepsilon}^{\mathrm{p},\beta}_{\mathrm{n+1}}\right]\right) \boldsymbol{n}^{\alpha\beta} = \boldsymbol{0}. \end{aligned} \tag{24}$$

Taking into account the Hadamard condition and the related equations, cf. Eqs. (7)–(11), the residuum can be formulated in terms of the total strain, the phase-specific plastic strains, and the jump vector, reading

$$\begin{aligned} \boldsymbol{g}^{\alpha\beta} = &\left(\left(\mathbb{C}^\alpha - \mathbb{C}^\beta\right)\left[\boldsymbol{\varepsilon}_{\mathrm{n+1}} - \phi_\alpha \boldsymbol{a}^{\alpha\beta}_{\mathrm{n+1}} \otimes \boldsymbol{n}^{\alpha\beta}\right] + \mathbb{C}^\alpha \left[\boldsymbol{a}^{\alpha\beta}_{\mathrm{n+1}} \otimes \boldsymbol{n}^{\alpha\beta}\right]\right) \boldsymbol{n}^{\alpha\beta} \\ &- \left(\mathbb{C}^\alpha \left[\boldsymbol{\varepsilon}^{\mathrm{p},\alpha}_{\mathrm{n+1}}\right] - \mathbb{C}^\beta \left[\boldsymbol{\varepsilon}^{\mathrm{p},\beta}_{\mathrm{n+1}}\right]\right) \boldsymbol{n}^{\alpha\beta} = \boldsymbol{0}. \end{aligned} \tag{25}$$

The more general case, accouting for more than two phases, is described in detail by, e.g., [54, 74]. Following Eq. (7) and (11), the phase-specific strains can be computed by means of the jump vector $\boldsymbol{a}^{\alpha\beta}_{\mathrm{n+1}}$. Due to

$$\tau_\xi^{n+1,\alpha} = \mathbb{C}^\alpha \left[\boldsymbol{\varepsilon}^\alpha_{\mathrm{n+1}}\left(\boldsymbol{a}^{\alpha\beta}_{\mathrm{n+1}}\right) - \boldsymbol{\varepsilon}^{\mathrm{p},\alpha}_{\mathrm{n+1}}\right] \cdot \boldsymbol{M}^\alpha_\xi \tag{26}$$

the residuals $\boldsymbol{g}^\alpha_1$, g^α_2, $\boldsymbol{g}^\beta_1$, and g^β_2 depend on vector $\boldsymbol{a}^{\alpha\beta}_{\mathrm{n+1}}$ as well.

3.3.2 Solution of the local problem

The solution of the system of nonlinear equations stated by the residuals $\boldsymbol{g}^\alpha_1$, g^α_2, $\boldsymbol{g}^\beta_1$, g^β_2, and $\boldsymbol{g}^{\alpha\beta}$ can be determined by means of a Newton procedure. In this regard, the following linearized system has to be solved

$$\begin{aligned} &\begin{bmatrix} \frac{\partial \boldsymbol{g}^\alpha_1}{\partial \boldsymbol{\varepsilon}^{\mathrm{p},\alpha}_{\mathrm{n+1}}} & \frac{\partial \boldsymbol{g}^\alpha_1}{\partial \gamma^\alpha_{\mathrm{ac,n+1}}} & \frac{\partial \boldsymbol{g}^\alpha_1}{\partial \boldsymbol{a}^{\alpha\beta}_{\mathrm{n+1}}} & 0 & 0 \\ \frac{\partial g^\alpha_2}{\partial \boldsymbol{\varepsilon}^{\mathrm{p},\alpha}_{\mathrm{n+1}}} & \frac{\partial g^\alpha_2}{\partial \gamma^\alpha_{\mathrm{ac,n+1}}} & \frac{\partial g^\alpha_2}{\partial \boldsymbol{a}^{\alpha\beta}_{\mathrm{n+1}}} & 0 & 0 \\ \frac{\partial \boldsymbol{g}^{\alpha\beta}}{\partial \boldsymbol{\varepsilon}^{\mathrm{p},\alpha}_{\mathrm{n+1}}} & 0 & \frac{\partial \boldsymbol{g}^{\alpha\beta}}{\partial \boldsymbol{a}^{\alpha\beta}_{\mathrm{n+1}}} & \frac{\partial \boldsymbol{g}^{\alpha\beta}}{\partial \boldsymbol{\varepsilon}^{\mathrm{p},\beta}_{\mathrm{n+1}}} & 0 \\ 0 & 0 & \frac{\partial \boldsymbol{g}^\beta_1}{\partial \boldsymbol{a}^{\alpha\beta}_{\mathrm{n+1}}} & \frac{\partial \boldsymbol{g}^\beta_1}{\partial \boldsymbol{\varepsilon}^{\mathrm{p},\beta}_{\mathrm{n+1}}} & \frac{\partial \boldsymbol{g}^\beta_1}{\partial \gamma^\beta_{\mathrm{ac,n+1}}} \\ 0 & 0 & \frac{\partial g^\beta_2}{\partial \boldsymbol{a}^{\alpha\beta}_{\mathrm{n+1}}} & \frac{\partial g^\beta_2}{\partial \boldsymbol{\varepsilon}^{\mathrm{p},\beta}_{\mathrm{n+1}}} & \frac{\partial g^\beta_2}{\partial \gamma^\beta_{\mathrm{ac,n+1}}} \end{bmatrix} \begin{bmatrix} \Delta \boldsymbol{\varepsilon}^{\mathrm{p},\alpha}_{\mathrm{n+1}} \\ \Delta \gamma^\alpha_{\mathrm{ac,n+1}} \\ \boldsymbol{a}^{\alpha\beta}_{\mathrm{n+1}} \\ \Delta \boldsymbol{\varepsilon}^{\mathrm{p},\beta}_{\mathrm{n+1}} \\ \Delta \gamma^\beta_{\mathrm{ac,n+1}} \end{bmatrix} \\ &= - \begin{bmatrix} \boldsymbol{g}^\alpha_1 \\ g^\alpha_2 \\ \boldsymbol{g}^{\alpha\beta} \\ \boldsymbol{g}^\beta_1 \\ g^\beta_2 \end{bmatrix}, \end{aligned} \tag{27}$$

within the Newton procedure. For a better applicability towards more than two phases, the terms $\partial \boldsymbol{g}^\alpha_1 / \partial \boldsymbol{a}^{\alpha\beta}_{\mathrm{n+1}}$, $\partial g^\alpha_2 / \partial \boldsymbol{a}^{\alpha\beta}_{\mathrm{n+1}}$, $\partial \boldsymbol{g}^\beta_1 / \partial \boldsymbol{a}^{\alpha\beta}_{\mathrm{n+1}}$, $\partial g^\beta_2 / \partial \boldsymbol{a}^{\alpha\beta}_{\mathrm{n+1}}$, $\partial \boldsymbol{g}^{\alpha\beta} / \partial \boldsymbol{\varepsilon}^{\mathrm{p},\alpha}_{\mathrm{n+1}}$, and $\partial \boldsymbol{g}^{\alpha\beta} / \partial \boldsymbol{\varepsilon}^{\mathrm{p},\beta}_{\mathrm{n+1}}$ are neglected and a quasi-Newton procedure is solved, instead. This approximation of the Jacobian from Eq. (27) yields a decoupling of the system of equations, reading

$$
\begin{bmatrix}
\frac{\partial \boldsymbol{g}_1^{\alpha}}{\partial \boldsymbol{\varepsilon}_{\mathrm{n+1}}^{\mathrm{p},\alpha}} & \frac{\partial \boldsymbol{g}_1^{\alpha}}{\partial \gamma_{\mathrm{ac,n+1}}^{\alpha}} & 0 & 0 & 0 \\
\frac{\partial g_2^{\alpha}}{\partial \boldsymbol{\varepsilon}_{\mathrm{n+1}}^{\mathrm{p},\alpha}} & \frac{\partial g_2^{\alpha}}{\partial \gamma_{\mathrm{ac,n+1}}^{\alpha}} & 0 & 0 & 0 \\
0 & 0 & \frac{\partial \boldsymbol{g}^{\alpha\beta}}{\partial \boldsymbol{a}_{\mathrm{n+1}}^{\alpha\beta}} & 0 & 0 \\
0 & 0 & 0 & \frac{\partial \boldsymbol{g}_1^{\beta}}{\partial \boldsymbol{\varepsilon}_{\mathrm{n+1}}^{\mathrm{p},\beta}} & \frac{\partial \boldsymbol{g}_1^{\beta}}{\partial \gamma_{\mathrm{ac,n+1}}^{\beta}} \\
0 & 0 & 0 & \frac{\partial g_2^{\beta}}{\partial \boldsymbol{\varepsilon}_{\mathrm{n+1}}^{\mathrm{p},\beta}} & \frac{\partial g_2^{\beta}}{\partial \gamma_{\mathrm{ac,n+1}}^{\beta}}
\end{bmatrix}
\begin{bmatrix}
\Delta \boldsymbol{\varepsilon}_{\mathrm{n+1}}^{\mathrm{p},\alpha} \\
\Delta \gamma_{\mathrm{ac,n+1}}^{\alpha} \\
\boldsymbol{a}_{\mathrm{n+1}}^{\alpha\beta} \\
\Delta \boldsymbol{\varepsilon}_{\mathrm{n+1}}^{\mathrm{p},\beta} \\
\Delta \gamma_{\mathrm{ac,n+1}}^{\beta}
\end{bmatrix}
= -
\begin{bmatrix}
\boldsymbol{g}_1^{\alpha} \\ g_2^{\alpha} \\ \boldsymbol{g}^{\alpha\beta} \\ \boldsymbol{g}_1^{\beta} \\ g_2^{\beta}
\end{bmatrix}. \tag{28}
$$

The linearized system according to Eq. (28) exhibits a block structure. Thus, the systems of equations, constituting the α- respectively β-block, and the $\boldsymbol{g}^{\alpha\beta}$-block can be solved independently of each other. The detailed solution of the local problem is schematically illustrated by the flowchart in Fig. 2. Both, the global and the local problems are solved by means of the in-house software suite PACE3D, cf., e.g., [84].

4 Numerical results

4.1 Comparison of approaches to plasticity in the multiphase-field context

4.1.1 Motivation

As discussed by [74] in the context of Mises plasticity, unphysical results are obtained by the CPFA within the diffuse interface region, if a high contrast of material parameters, such as the yield stress, is considered. In contrast to Mises plasticity, the lattice orientation of each grain is taken into account by crystal plasticity. Thus, regarding two adjacent phases of different lattice orientation, the orientation of the lattice within the diffuse interface region is given as an interpolation between the orientations of the adjacent phases, in the context of the CPFA, cf., e.g., [77, Fig. 1 (b)]. Consequently, artificial intermediate orientations enter the diffuse interface region, that are not present in the non-regularized, SI context. In this regard, it is desirable to compare results obtained for the SI theory with those obtained for the CPFA and the PSPFA. To mimic the implementation of the CP theory within the CPFA, a SI set-up is considered exhibiting discrete intermediate orientations within the domain that is considered to be the diffuse interface within the PSPFA. Subsequently, the results obtained for the SI theory are compared to results of the PSPFA within the PFM.

4.1.2 Boundary conditions and material parameters

Subsequently, the following Neumann boundary conditions

$$
\begin{aligned}
&\bar{\boldsymbol{t}}\,(x, \pm H/2, z) = \bar{\boldsymbol{t}}\,(x, y, \pm B/2) = \boldsymbol{0}, \\
&\bar{\boldsymbol{t}}\,(\pm L/2, y, z) \cdot \boldsymbol{e}_y = \bar{\boldsymbol{t}}\,(\pm L/2, y, z) \cdot \boldsymbol{e}_z = 0
\end{aligned} \tag{29}
$$

as well as the Dirichlet boundary conditions

$$
\boldsymbol{u}\,(-L/2, y, z) \cdot \boldsymbol{e}_x = 0, \quad \boldsymbol{u}\,(L/2, y, z) \cdot \boldsymbol{e}_x = u_0 \tag{30}
$$

are applied. The Dirichlet boundary condition u_0 is chosen such that $\varepsilon_{xx} = 0.02$ holds true. The domain is discretized by $300 \times 43 \times 43$ cells regarding the $\boldsymbol{e}_x$, $\boldsymbol{e}_y$, and $\boldsymbol{e}_z$-direction, using an equidistant, Cartesian grid (Fig. 3).

For the subsequent simulations, the material parameters according to Table 2 are applied. In this regard, an elastically isotropic material is considered with E denoting Young's modulus and ν Poisson's ratio.

4.1.3 Crystallographic orientations

Subsequently, FCC crystals are considered, exclusively. The orientation of the crystal lattice, and, thus, of the crystal grain, is described with respect to a ⟨100⟩-oriented grain, by means of a set of Bryant-angles $\mathcal{O} = \{\psi_{\mathrm{x}}, \psi'_{\mathrm{y}}, \psi''_{\mathrm{z}}\}$, cf., e.g., [86, p. 351]. Regarding an initial $\{\boldsymbol{e}_x, \boldsymbol{e}_y, \boldsymbol{e}_z\}$-coordinate system, ψ_{x} describes the rotation around the $\boldsymbol{e}_x$-axis, yielding the $\{\boldsymbol{e}'_x, \boldsymbol{e}'_y, \boldsymbol{e}'_z\}$-coordinate system. The rotation around the $\boldsymbol{e}'_y$-axis is described by ψ'_{y} leading to the $\{\boldsymbol{e}''_x, \boldsymbol{e}''_y, \boldsymbol{e}''_z\}$-coordinate system. Consequently, the rotation around the $\boldsymbol{e}''_z$-axis is denoted by ψ''_{z}. All rotations are carried out counter clockwise with respect to the corresponding rotation axis. Thus, $\mathcal{O} = \{0, \psi'_{\mathrm{y}}, 0\}$ describes the rotation of the crystal lattice around the $\boldsymbol{e}'_y$-axis, which corresponds to the $\boldsymbol{e}_y$-axis since $\psi_{\mathrm{x}} = 0$ holds true, by the angle ψ'_{y}. Regarding an ideally oriented ⟨100⟩-grain, the ⟨100⟩-directions of the crystal are aligned with the coordinate axes, cf., e.g., [18].

4.1.4 Bicrystal study illustrating the SI solution

At first, a bicrystal set-up is considered to illustrate the comparison of the SI solution with the CPFA and the PSPFA. The orientations $\mathcal{O}_{\mathrm{L}}$ and $\mathcal{O}_{\mathrm{R}}$ of the left grain (blue) and the right grain (red) are given by $\mathcal{O}_{\mathrm{L}} = \{0°, -13°, 0°\}$ and $\mathcal{O}_{\mathrm{R}} = \{0°, 13°, 0°\}$, respectively, cf. Fig. 4a. Thus, the lattices are rotated by $-13°$ respectively $13°$ around the $\boldsymbol{e}_y$-axis with respect to the ⟨100⟩-orientation. The bicrystal is depicted with respect to the deformed state in Fig. 5a, regarding the $\boldsymbol{e}_x$-$\boldsymbol{e}_z$-plane, and (d), regarding the $\boldsymbol{e}_x$-$\boldsymbol{e}_y$-plane,

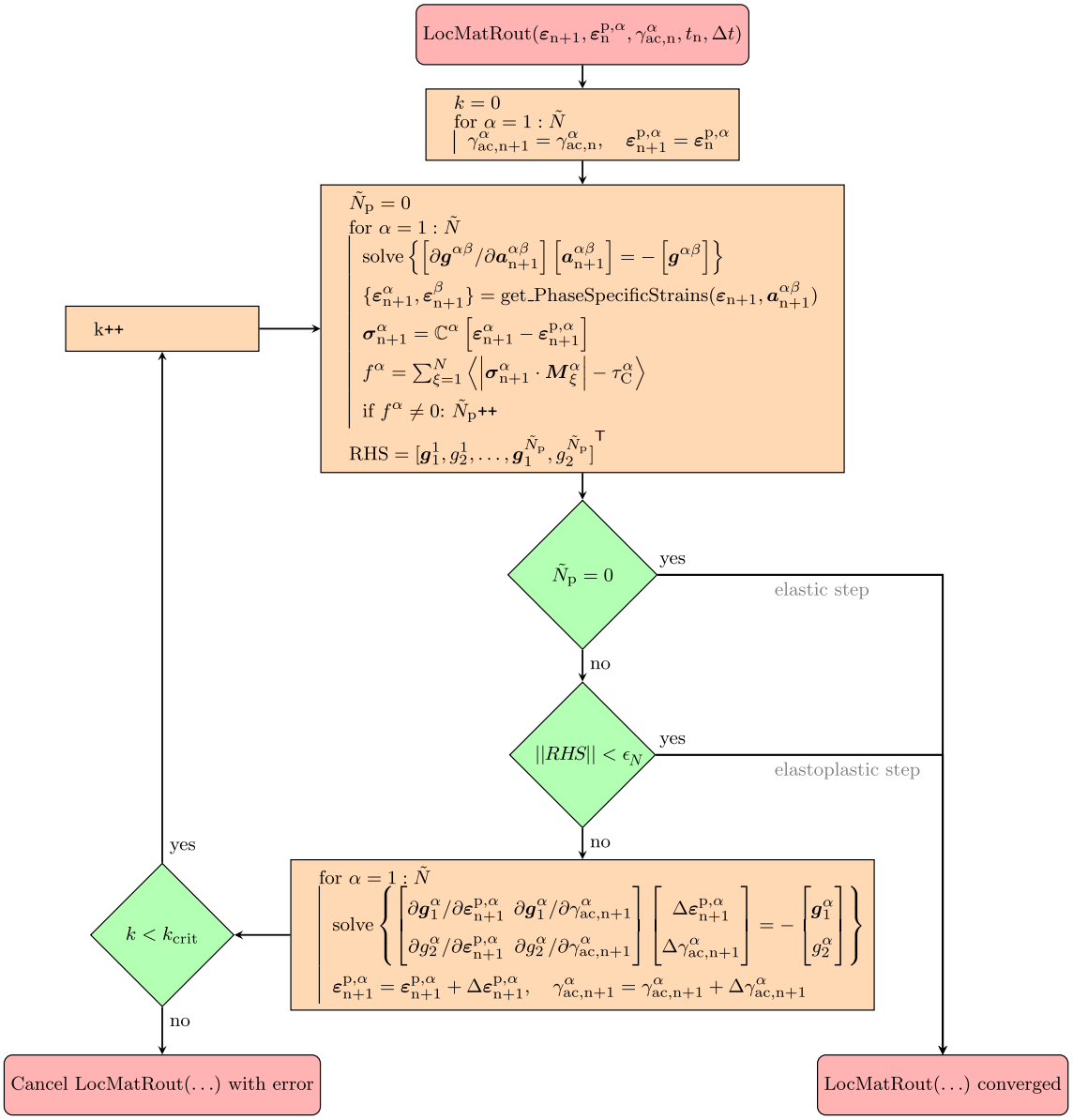

Fig. 2 Schematic flowchart regarding the solution of the local problem within the diffuse interface region. Here, k represents the iteration index of the while loop, $\tilde{N}$ the number of adjacent phases, $\tilde{N}_p$ the number of the adjacent phases that are plastically active, ϵ_N the accuracy threshold for the convergence of the local quasi-Newton procedure, and k_{crit} the maximum number of iterations

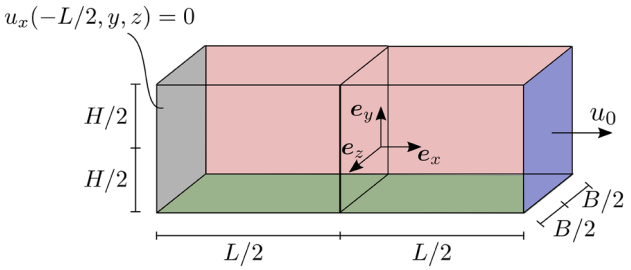

Fig. 3 Schematic representation of the Dirichlet boundary conditions that apply to all simulations performed in the present work

illustrating the accumulated plastic slip and the Mises stress after the deformation in the left and right column, respectively. For a better analysis, the deformation is depicted using a warp factor of 10. Within the $\boldsymbol{e}_x$-$\boldsymbol{e}_z$-plane, a shearing of the bicrystal is observed caused by the plastic anisotropy induced by the slip system orientations. Both the accumulated plastic strain and the Mises stress are homogeneous throughout the domain. Within the $\boldsymbol{e}_x$-$\boldsymbol{e}_y$-plane, no shearing is observable. The SI solution is considered as a benchmark for both the CPFA and the PSPFA.

Table 2 Material parameters considered for all simulations, in the work at hand, based on [85]

E in MPa	ν in [−]	τ_0^{C} in MPa	τ_∞^{C} in MPa	τ^{D} in MPa	m in −	$\dot{\gamma}_0$ in s^{-1}	Θ_0 in MPa
$65 \cdot 10^3$	0.347	30	108	1	8	10^{-3}	1075

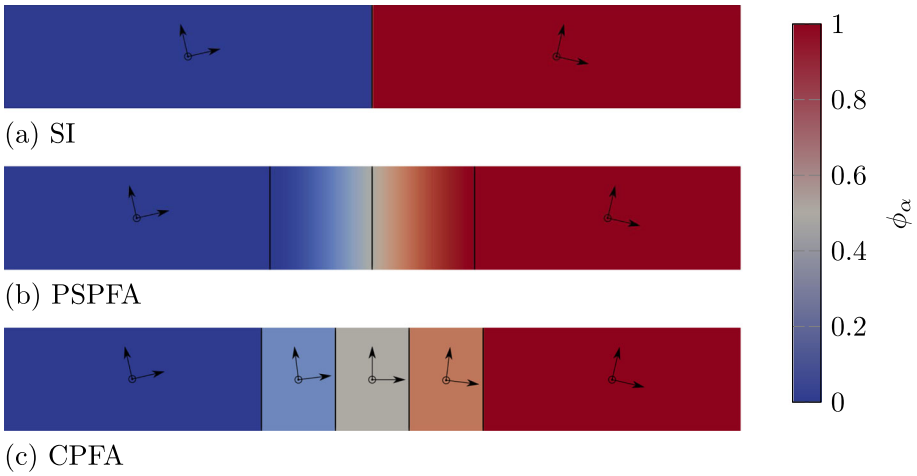

Fig. 4 Schematic illustration of the phases (subregions) considered with respect to the simulations of the bicrystal **a** in the SI context, **b** the PSPFA, **c** the CPFA. The location of the SI is illustrated by the black line, separating the blue and red region in (**a**). Regarding the PSPFA, the diffuse interface region is illustrated by the two square regions left and right of the SI in (**b**). Mimicking the CPFA, three discrete intermediate orientations (**c**) are introduced in the region that is considered to be diffuse in the PSPFA

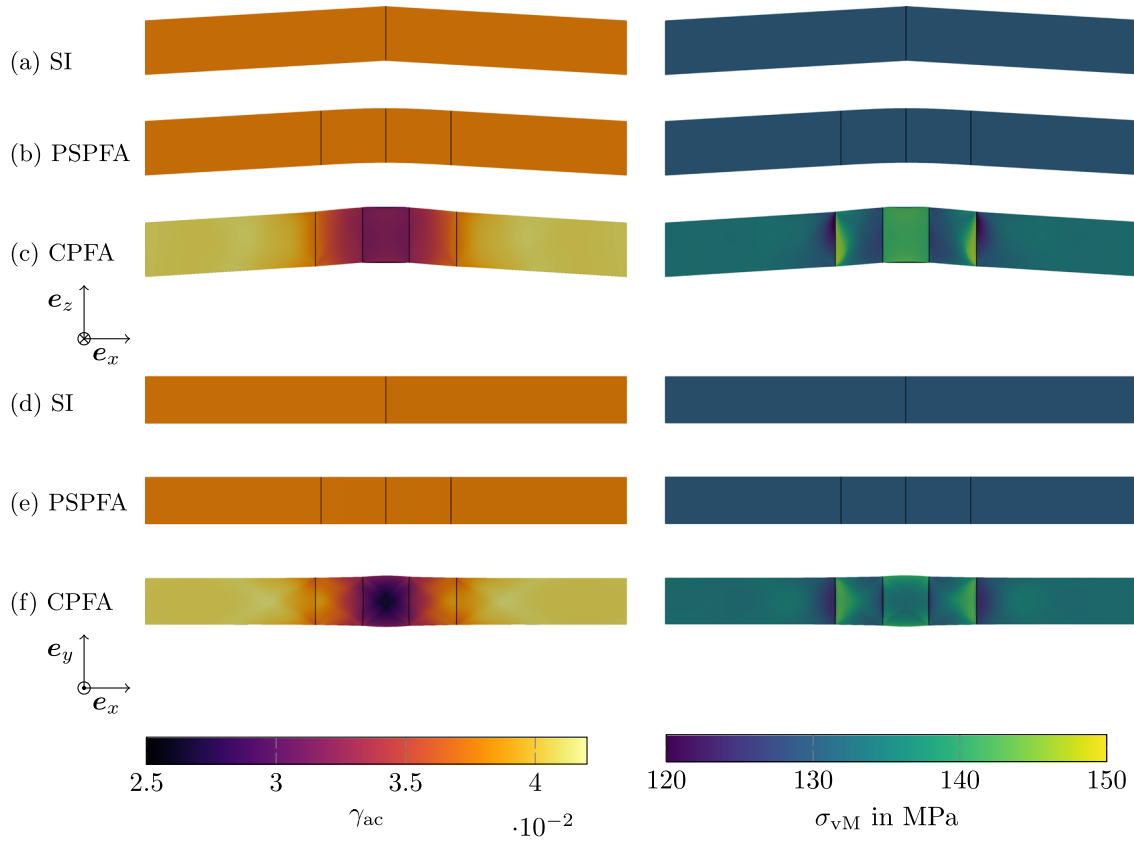

Fig. 5 Distribution of the accumulated plastic slip (left column) and the Mises stress (right column) obtained in the context of **a**, **d** the SI theory, **b**, **e** the PSPFA, and **c**, **f** the CPFA, with respect to the $\boldsymbol{e}_x$-$\boldsymbol{e}_z$-plane and the $\boldsymbol{e}_x$-$\boldsymbol{e}_y$-plane. Regarding the PSPFA, the accumulated plastic slip and the Mises stress within the diffuse interface region, marked by the two outer vertical solid lines in (**b**, **e**), are given by the interpolation of the phase-specific distributions as $\gamma_{\mathrm{ac}} = \sum_\alpha \phi_\alpha \gamma_{\mathrm{ac}}^\alpha$ and $\sigma_{\mathrm{vM}} = \sum_\alpha \phi_\alpha \sigma_{\mathrm{vM}}^\alpha$, respectively. In the context of the CPFA, the oligocrystalline character of the result induced by the artificially introduced intermediate orientations is clearly visible. The distribution of the accumulated plastic slip as well as the Mises stress obtained by the mimicked CPFA significantly differs from the SI solution both qualitatively and quantitatively, not only within the diffuse interface region, but within the overall simulation domain. The solutions obtained by the implementation within the PSPFA coincide with the SI solution

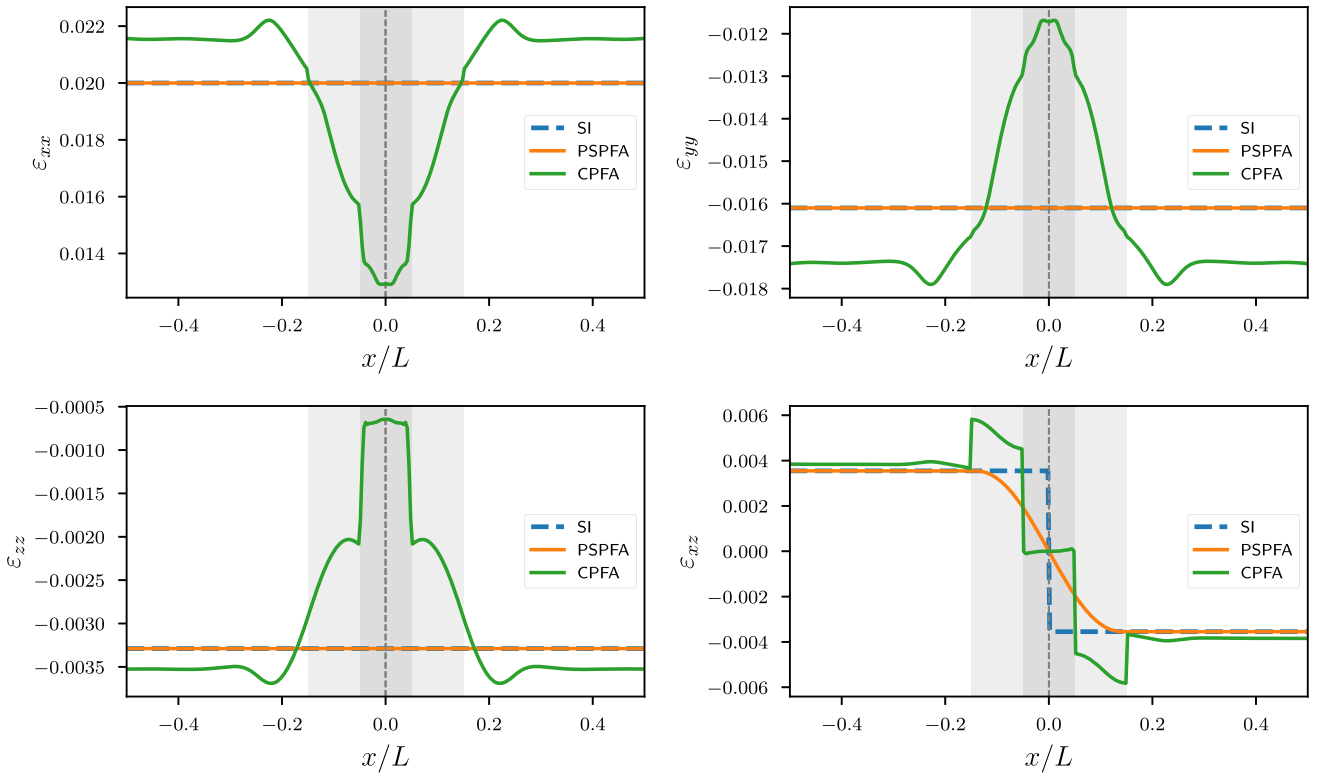

Fig. 6 Distribution of the (numerically) non-vanishing components of the total strain along the $\boldsymbol{e}_z$-axis, i.e., given by $x = 0, y = 0$ for variable z. The distribution obtained for the PSPFA and the SI theory coincide regarding the diagonal components. The xz-component obtained for the PSPFA represents the classical phase-field approximation of the SI solution. In contrast, the distribution obtained in the context of the CPFA differs significantly from the SI, for all non-vanishing components of the total strain. Especially the xz-component of the CPFA-solution illustrates the artificially introduced intermediate orientations considered by the CPFA

4.1.5 Bicrystal study illustrating CPFA

In the context of the CPFA, the orientation of the crystal lattice between the left and the right grain is interpolated. To mimic this, three intermediate configurations, referred to as $\mathcal{O}_{\mathrm{ML}}$, $\mathcal{O}_{\mathrm{M}}$, and $\mathcal{O}_{\mathrm{MR}}$, are introduced within the region which is considered to be the diffuse interface region, illustrated by the two outer vertical lines in Fig. 4b, for the subsequent PSPFA. The orientations considered are given from left to right as $\mathcal{O}_{\mathrm{L}} = \{0°, -13°, 0°\}$, $\mathcal{O}_{\mathrm{ML}} = \{0°, -7°, 0°\}$, $\mathcal{O}_{\mathrm{M}} = \{0°, 0°, 0°\}$, $\mathcal{O}_{\mathrm{MR}} = \{0°, 7°, 0°\}$, and $\mathcal{O}_{\mathrm{R}} = \{0°, 13°, 0°\}$. Regarding Fig. 4c, the diffuse interface region is located between the dark blue and the dark red grains. The intermediate configurations are colored in light blue, grey and light red. Figure 5f shows a thickening of the unrotated center grain within the $\boldsymbol{e}_x$-$\boldsymbol{e}_y$-plane, which is not present in the SI context, cf. Fig. 5d. In addition, the distribution of both the accumulated plastic slip and the Mises stress, as illustrated by Fig. 5c, f, left and right column, is not homogeneous within the diffuse interface region as for the SI solution. To compare the overall kinematical behavior of the CPFA and the SI solution, the non-vanishing strains are plotted along the neutral axis, i.e., along the $\boldsymbol{e}_x$-axis for $y = 0$ and $z = 0$ in Fig. 6. In this context, the region of the diffuse interface is highlighted in grey. The two light grey areas correspond to the regions, where $\mathcal{O}_{\mathrm{ML}}$ and $\mathcal{O}_{\mathrm{MR}}$ are applied in the context of CPFA, the dark grey area to the region where $\mathcal{O}_{\mathrm{M}}$ is applied. The strains obtained by means of the SI solution are depicted in blue, the strains obtained by the CPFA in green. For all depicted strains, a significant deviation of the CPFA from the SI solution is observed. Especially the deviation of the shear strain ε_{xz}, depicted in the right lower image of Fig. 6, illustrates the three artificial, intermediate configurations introduced by the CPFA. These deviations are not limited to the mimicked diffuse interface region but are present throughout the whole simulation domain. At a certain distance from the diffuse interface region, an approximately constant deviation from the SI solution is observed. This behavior is also present, if the width L_δ of the interface is reduced. To illustrate this, the distributions of ε_{xx} and ε_{xz}, obtained for the SI theory, the PSPFA, and the CPFA, are depicted along the $\boldsymbol{e}_x$-axis for $y = 0$ and $z = 0$ in Fig. 7. For the CPFA and the PSPFA, three interface widths are considered: $L_\delta = 0.1L$, $L_\delta = 0.2L$, and $L_\delta = 0.3L$, with L

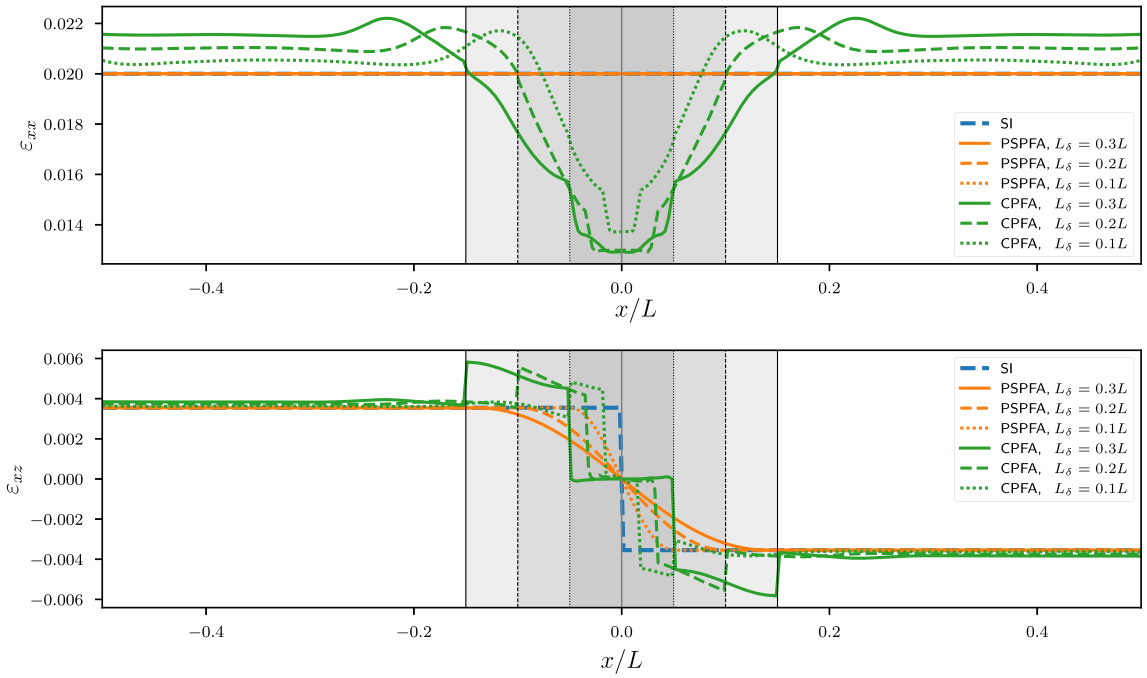

Fig. 7 The influence of the interface width L_δ on the distributions of ε_{xx} and ε_{xz}, along the $\boldsymbol{e}_x$-axis for $y = 0$ and $z = 0$, is illustrated. To this end, $L_\delta = 0.1L$, $L_\delta = 0.2L$, $L_\delta = 0.3L$ are considered, with L denoting the length of the bicrystal. Regarding the CPFA, the distribution of ε_{xx} clearly deviates from the SI solution inside and outside of the diffuse interface region, even for a reduced interface width. The deviation is both qualitative and quantitative in nature. For the PSPFA, the distribution of ε_{xx} conincides with the SI solution and is, thereby, not affected by the change of the interface width L_δ. The distribution of ε_{xz} is only affected within the diffuse interface region. A reduction of L_δ squeezes the distribution together. Outside of the diffuse interface region, it coincides with the SI solution and is not affected by the variation in L_δ

denoting the length of the bicrystal. Thus, the effect of a reduction of the interface width $L_\delta = 0.3L$, used for the results depicted in Figs. 5 and 6, to two thirds and one third on the distribution of the strain components is depicted. Especially for ε_{xx}, the distribution obtained for CPFA clearly deviates from the from the SI solution, both quantitatively and qualitatively, even outside the diffuse interface. Regarding the PSPFA, the distribution of ε_{xx} is not affected by a reduction of the interface width at all. The distribution of ε_{xy} is only affected within the diffuse interface region in the sense that it is squeezed together. However, outside the diffuse interface region it coincides with the solution of the SI theory. Summarizing, neither the distribution of the accumulated plastic slip or the Mises stress nor the deformation behavior obtained in the context of the CPFA is in accordance with the SI solution. The mimicked CPFA leads to the behavior of an oligocrystal, consisting of five differently oriented grains, and, thus, to a completely different simulation set-up as considered in the SI context. An implementation of the CPFA yields more intermediate orientations than the three that are considered in the mimicking set-up, leading to an increased heterogeneity of the material behavior within the diffuse interface region. Consequently, the implementation of the CP theory within the CPFA is not recommended. Moreover, this recommendation was also deduced with respect to other material behaviors, such as viscoelasticity, as discussed by [83, Fig. 8–10], where aspects as physical and numerical interface width are examined.

4.1.6 Bicrystal study illustrating the PSPFA

Regarding the PSPFA, described in Sect. 3.3 and schematically illustrated by Fig. 2, only the two orientations $\mathcal{O}_\mathrm{L} = \{0°, -13°, 0°\}$ and $\mathcal{O}_\mathrm{R} = \{0°, 13°, 0°\}$ are considered, as in the SI context, cf. Fig. 4b. The width of the diffuse interface is the same as considered for the CPFA. In accordance with the SI solution, the bicrystal does not exhibit a thickening regarding the $\boldsymbol{e}_x$-$\boldsymbol{e}_y$-plane, cf. Fig. 5e. In addition the distributions of the accumulated plastic slip and the Mises stress are homogeneous as illustrated by Fig. 5b, e, left and right column, and thus, in accordance with the SI solution, cf. Fig. 5b, e, left and right column. The comparison of the non-vanishing strains regarding the PSPFA and the SI solution is illustrated in Fig. 6. The strains obtained for the PSPFA are depicted in orange while the strains of the SI solution are depicted in blue. Regarding $\varepsilon_{xx}, \varepsilon_{yy}, \varepsilon_{zz}$, the results of the PSPFA and the SI are identical. With respect to ε_{xz}, the PSPFA exhibits the classical diffuse interface approximation of the SI solution

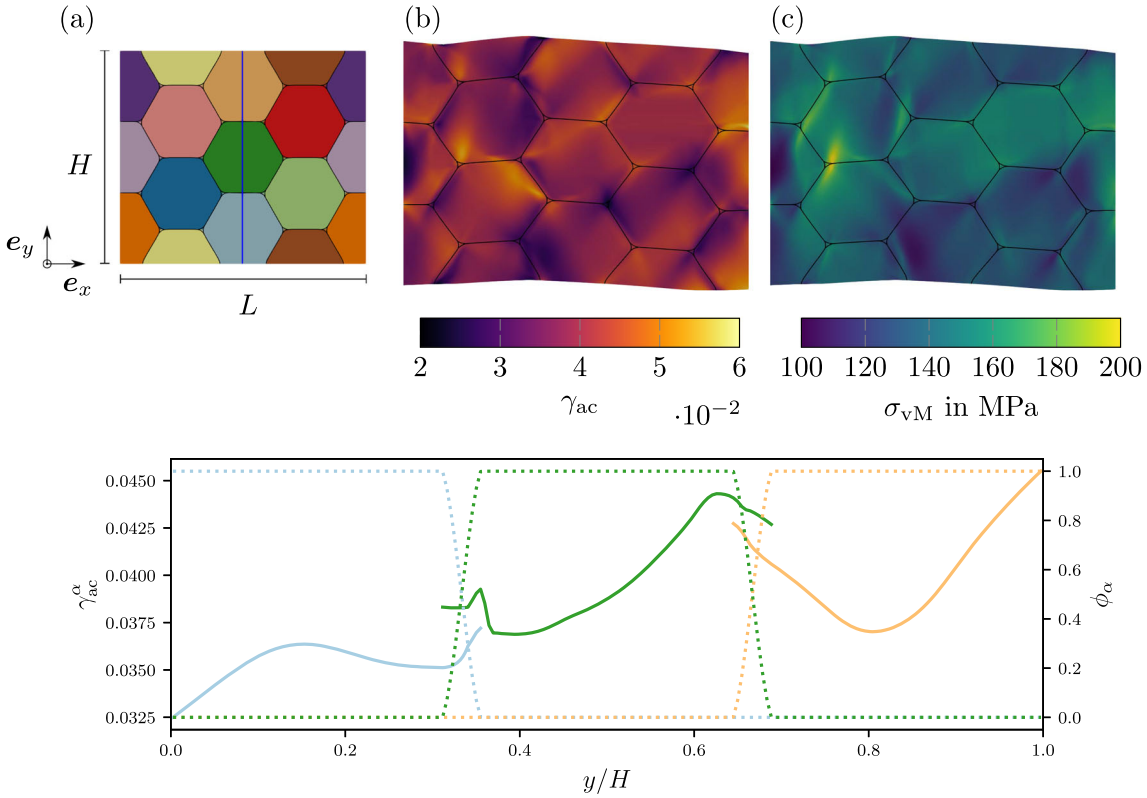

Fig. 8 Upper row: The implementation of the CP theory in terms of the PSPFA is applied to a structure resembling periodically arranged grains. The different orientations of the grains are illustrated by the different colors in the left picture. In contrast to the bicrystal benchmark discussed before, the diffuse interfaces, representing the grain boundaries between the grains, are considered significantly thinner, here. The boundary conditions applied are the same as considered in the context of the bicrystal benchmark, given by Eq. (30). The distribution of the accumulated plastic slip is displayed in the center picture, the distribution of the Mises stress σ_{vM} in the right picture. The inhomogeneous distributions are due to the different grain orientations and, thus, differently activated slip systems. Both the picture in the center and the right picture illustrate the displacement by a warp factor of 10. Lower row: The distributions of the phase-wise accumulated plastic slip (solid lines) as well as the distribution of the order parameters (dotted lines) are plotted along the vertical cut through the center of area of the honeycomb, illustrated by a blue line in the left picture of the upper row, from the lower boundary to the upper boundary. The width of the diffuse interface is chosen significantly smaller than for the previously considered bicrystal. This plot illustrates that the phase-specific accumulated plastic slip γ^{α}_{ac} is computed throughout the whole diffuse interface. The interpolation of the phase-specific accumulated plastic slip, given by $\gamma_{ac} = \sum_{\alpha} \phi_{\alpha} \gamma^{\alpha}_{ac}$, is depicted in the second picture of the upper row

which is characterized by a jump of ε_{xz} at the grain boundary between the left and the right grain. Consequently, both the distribution of the accumulated plastic slip respectively the Mises stress and the deformation behavior of the SI solution are reflected by the PSPFA, even for an interface of finite thickness. Finally, this benchmark motivates the implementation of the crystal plasticity according to the PSPFA within the multiphase-field context. Thus, the subsequent simulations are all carried out concerning the PSPFA.

4.2 Application to mutliple phases and more complex morphologies

4.2.1 Honeycomb structure

The implementation of the crystal plasticity accounting for the PSPFA is applied to a structure of grains resembling periodically arranged honeycombs, cf. the left image of Fig. 8. For the honeycomb structure, the orientations are chosen as $\mathcal{O}_{\alpha} = \{0°, 0°, \psi_{\alpha}\}$, such that the grains are rotated by random angles around the out-of-plane axis. The boundary conditions applied are chosen according to Eqs. (29) and (30). The discretization is $240 \times 207 \times 5$ cells regarding the $\boldsymbol{e}_x$, $\boldsymbol{e}_y$, and $\boldsymbol{e}_z$-direction using an equidistant, Cartesian grid. Both the distribution of the Mises stress, depicted in Fig. 8b, and the distribution of the accumulated plastic strain, depicted in Fig. 8c, are inhomogeneous due to the individual rotations of the grains. This is also reflected by the heterogeneous deformation behavior at the top and bottom of the honeycomb structure, which is graphically highlighted by using a warp factor of 10. A vertical cut through the center of area of the honeycomb-structure is illustrated by the blue line in Fig. 8a. Following the line from the bottom to the top, the phase-wise distributions of the accumulated

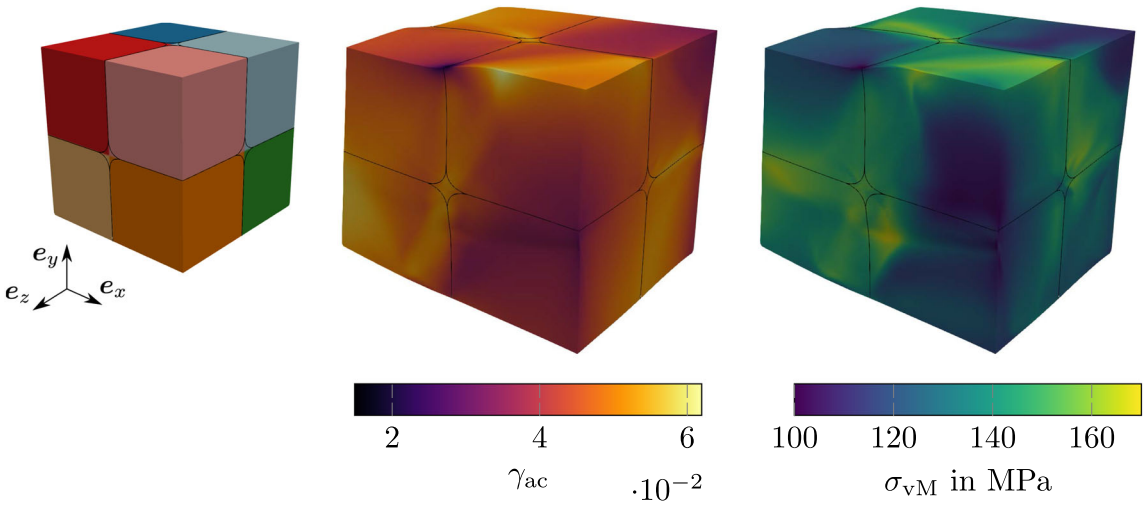

Fig. 9 The implementation of the CP theory in terms of the PSPFA is applied to an aggregate of eight grains referred to as octotuple. Each of the grains is assigned a random orientation. In contrast to the honeycomb strucutre, not only the rotation angle, but also the rotation axis characteristic for the respective orientation, is chosen randomly. The different orientations of the grains are illustrated by the different colors in the left picture. Similar to the honeycomb structure, the diffuse interfaces, representing the grain boundaries between the grains, are considered significantly thinner compared to the bicrystal benchmark. The boundary conditions applied are the same as considered in the context of the bicrylstal benchmark, given by Eq. (30). The distribution of the accumulated plastic slip is displayed in the center picture, the distribution of the Mises stress σ_{vM} in the right picture. The inhomogeneous distributions are due to the different grain orienations and, thus, differently activated slip systems. The picture in the center as well as the right picture illustrate the displacement by a warp factor of 10

plastic slips γ_{ac}^{α}, depicted as solid lines, and the distributions of the order paremeter, depicted as dotted lines, are illustrated in the lower row of Fig. 8. It is shown that the distribution of the phase-specific plastic slips γ_{ac}^{α} is computed over the entire diffuse interface domain for each locally present phase. Regarding Fig. 8b, the interpolation $\gamma_{ac} = \sum_{\alpha} \phi_{\alpha} \gamma_{ac}^{\alpha}$ is considered within the diffuse interface. The distribution of the order parameters illustrate that the width of the diffuse interface is chosen significantly smaller than for the bicrystal illustrated in Fig. 4b.

4.2.2 Octotuple

The application to more complex three-dimensional morphologies is demonstrated by applying the new approach to a grain aggregate consisting of eight grains with different orientations, briefly referred to as octotuple, cf. Fig. 9, left image. The boundary conditions are again chosen according to Eqs. (29) and (30) and each color represents an individual orientation. In contrast to the previous simulations, each grain is rotated according to $\mathcal{O}_{\alpha} = \{\psi_{\alpha,x}, \psi'_{\alpha,y}, \psi''_{\alpha,z}\}$ with randomly chosen rotation angles. The discretization is $90 \times 90 \times 90$ cells regarding the $\boldsymbol{e}_x$, $\boldsymbol{e}_y$, and $\boldsymbol{e}_z$-direction on an equidistant, Cartesian grid. The distribution of the Mises stress and the accumulated plastic strain, cf. Fig. 9, are both inhomogeneous. It has to be pointed out that eight different phases are present within the diffuse region at the center of the octotuple.

5 Concluding remarks

In the work at hand, a new multiphase-field approach to small strain crystal plasticity is presented, accounting for balance equations on singular surfaces. In this context, the implementation of the small strain CP theory is discussed with respect to both the bulk material as well as the diffuse interface region. A schematic but detailed illustration of the algorithm for points within the diffuse interface is provided by a flowchart. Benchmark simulations are presented comparing the approaches to the implementation of small strain CP in the multiphase-field context. In this context, the following simulations and corresponding results are discussed.

- Three-dimensional simulations regarding a bicrystal are carried out with respect to a sharp-interface set-up, a set-up mimicking the CPFA, and the PSPFA-implementation. The two grains of the bicrystal are assigned different orientations.
- Regarding PSPFA-implementation, the accumulated plastic slip, the Mises stress, and the volumetric strain components are identical to the SI solution, even for a finite thickness of the diffuse interface region. The non-vanishing shear component of the PSPFA-solution represents the phase-field approximation of the corresponding component of the SI solution.
- Regarding the set-up mimicking the CPFA, the solution in terms of the accumulated plastic slip and the Mises

stress exhibits large deviations with respect to the SI solution. In addition, the distributions of the volumetric strain components as well as the non-vanishing shear component significantly differ from the SI solution. This deviation is not limited to the diffuse interface region, but is present throughout the simulation domain. The CPFA leads to artificial intermediate lattice orientations within the diffuse interface region and, thereby, to an unphysical heterogeneous material behavior.

- The influence of the interface width on the strain is exemplarily discussed with respect to the distributions of ε_{xx} and ε_{xz}. The distribution obtained for the CPFA still clearly deviates from the SI solution inside and outside the diffuse interface region, even for a reduced interface width.
- In consequence, the implementation of the CP theory in the multiphase-field context is not recommended in terms of CPFA, but in terms of PSPFA.
- The application of the CP in terms of PSPFA to more complex microstructures is illustrated by simulations of a periodic honeycomb structure and an octotuple, a grain aggregate consisting of eight differently oriented grains.

Acknowledgements Andreas Prahs gratefully acknowledges the financial support of KIT excellence strategy KIT ExU-Future Fields Stage 3 “Kadi4Mat”. Lukas Schöller and Felix Schwab gratefully acknowledge the financial support by the Deutsche Forschungsgemeinschaft (DFG, German Research Foundation), project number 255730231, within the International Research Training Group "Integrated engineering of continuous-discontinuous long fiber reinforced polymer structures" (GRK 2078/2). Lukas Schöller, Daniel Schneider, and Britta Nestler gratefully acknowledge the financial support of "Materials Science and Engineering (MSE)" programme No. 43.31.01, supported by the Helmholtz association. Thomas Böhlke gratefully acknowledges the financial support of KIT excellence strategy KIT ExU-Future Fields Stage 2 "ACDC". Andreas Prahs, Daniel Schneider, and Britta Nestler also gratefully acknowledge the support from KIT excellence strategy KIT ExU-Future Fields Stage 2 "ACDC", enabling meetings for intensive intellectual exchange on continuum thermodynamics.

Funding Open Access funding enabled and organized by Projekt DEAL.

Appendix A

A.1 Thermodynamical consistent modeling of (classical) crystal plasticity

A.1.1 Exploitation of the Clausius–Duhem inequality in regular points

The assumptions considered subsequently, regarding the thermodynamically consistent crystal plasticity framework correspond, e.g., to the assumptions considered by [62, A. 1-3 & A6-11], thereby representing a thermomechanically weakly coupled theory [87]. Accounting for these assumptions and applying the material time derivative to the specific free energy, the Clausius–Duhem inequality reads

$$\rho\delta = \left(\boldsymbol{\sigma} - \rho\frac{\partial\psi_\mathrm{e}}{\partial\boldsymbol{\varepsilon}}\right)\cdot\dot{\boldsymbol{\varepsilon}} - \sum_{\xi=1}^{N}\left(\rho\frac{\partial\psi_\mathrm{e}}{\partial\boldsymbol{\varepsilon}^\mathrm{p}}\cdot\frac{\partial\boldsymbol{\varepsilon}^\mathrm{p}}{\partial\gamma_\xi}\dot{\gamma}_\xi\right) - \rho\frac{\partial\psi_\mathrm{h}}{\partial\gamma_\mathrm{ac}}\dot{\gamma}_\mathrm{ac} - \rho\left(\eta + \frac{\partial\psi_\theta}{\partial\theta}\right)\dot{\theta} - \frac{1}{\theta}\boldsymbol{q}\cdot\boldsymbol{g} \geq 0. \tag{A1}$$

Following the procedure according to [88], the CDI has to be valid for arbitrary rates and their gradients [88, Eqs. (5.11)–(5.14)]. Considering, $-\rho\partial\psi_\mathrm{e}/\partial\boldsymbol{\varepsilon}^\mathrm{p} = \rho\partial\psi_\mathrm{e}/\partial\boldsymbol{\varepsilon}$, $\partial\boldsymbol{\varepsilon}^\mathrm{p}/\partial\gamma_\xi = \boldsymbol{M}_\xi$, and $\tau_\xi = \boldsymbol{\sigma}\cdot\boldsymbol{M}_\xi$ the Cauchy stress and the entropy are given by potential relations $\boldsymbol{\sigma} = \rho\partial\psi_\mathrm{e}/\partial\boldsymbol{\varepsilon}$ and $\eta = -\partial\psi_\theta/\partial\theta$, and a reduced dissipation inequality is obtained, reading

$$\rho\delta = \rho\delta_\mathrm{m} + \rho\delta_\theta \geq 0, \quad \rho\delta_\mathrm{m} = \sum_{\xi=1}^{N}\left(\tau_\xi\dot{\gamma}_\xi - \rho\frac{\partial\psi_\mathrm{h}}{\partial\gamma_\mathrm{ac}}\left|\dot{\gamma}_\xi\right|\right),$$
$$\rho\delta_\theta = -\frac{1}{\theta}\boldsymbol{q}\cdot\boldsymbol{g}. \tag{A2}$$

Since no coupling is present between δ_m and δ_θ, $\rho\delta_\mathrm{m} \geq 0$ and $\rho\delta_\theta \geq 0$ have to be ensured. Introducing the critical resolved shear stress as $\tau_\mathrm{C} := \rho\partial\psi_\mathrm{h}/\partial\gamma_\mathrm{ac} + \tau_0$, with $\tau_0 > 0$, the dissipation inequalities read

$$\rho\delta_\mathrm{m} = \sum_{\xi=1}^{N}\left(\tau_\xi\ \mathrm{sgn}\left(\dot{\gamma}_\xi\right) - \left(\tau_\mathrm{C} - \tau_0\right)\right)\left|\dot{\gamma}_\xi\right| \geq 0,$$
$$\rho\delta_\theta = -\frac{1}{\theta}\boldsymbol{q}\cdot\boldsymbol{g} \geq 0. \tag{A3}$$

The non-negativity of the δ_θ is ensured by assuming Fourier’s law, reading $\boldsymbol{q} = -\boldsymbol{K}\boldsymbol{g}$, cf., e.g., [89]. In this context, $\boldsymbol{K}$ refers to the heat conduction tensor, which is positive definite.

A.1.2 Flow rule and yield condition

Subsequently, a rate-dependent, i.e. viscous, flow rule of overstress type is considered, reading

$$\dot{\gamma}_\xi = \dot{\gamma}_0 \left\langle \frac{|\tau_\xi| - \tau_\mathrm{C}}{\tau_\mathrm{D}} \right\rangle^m \operatorname{sgn}(\tau_\xi) \tag{A4}$$

cf., e.g., [67, Eq. (1.16)]. Here, the referential shear rate is denoted by $\dot{\gamma}_0 > 0$, the strain rate sensitivity exponent by $m > 0$, the drag stress by $\tau_\mathrm{D} > 0$. The Macaulay brackets, defined by $\langle a \rangle := (a + |a|)/2$, are used, where a is an arbitrary scalar. The flow rule implies $\operatorname{sgn}(\tau_\xi) = \operatorname{sgn}(\dot{\gamma}_\xi)$. Inserting Eq. (A4) in Eq. (A3) illustrates that the considered flow rule Eq. (A4) fulfills the mechanical dissipation inequality

$$\begin{aligned}\rho\delta_\mathrm{m} &= \sum_{\xi=1}^{N} \left(|\tau_\xi| \operatorname{sgn}(\tau_\xi) \operatorname{sgn}(\dot{\gamma}_\xi) - (\tau_\mathrm{C} - \tau_0) \right) \dot{\gamma}_0 \left\langle \frac{|\tau_\xi| - \tau_\mathrm{C}}{\tau_\mathrm{D}} \right\rangle^m |\operatorname{sgn}(\tau_\xi)| \\ &= \dot{\gamma}_0 \sum_{\xi=1}^{N} \left((|\tau_\xi| - \tau_\mathrm{C}) \left\langle \frac{|\tau_\xi| - \tau_\mathrm{C}}{\tau_\mathrm{D}} \right\rangle^m + \tau_0 \left\langle \frac{|\tau_\xi| - \tau_\mathrm{C}}{\tau_\mathrm{D}} \right\rangle^m \right) \geq 0.\end{aligned} \tag{A5}$$

The numerator of Eq. (A4) defines the yield condition f as $f = |\tau_\xi| - \tau_\mathrm{C} \leq 0$. By means of Eq. (A4), the accumulated plastic slip reads

$$\dot{\gamma}_\mathrm{ac} = \sum_{\xi=1}^{N} \left| \dot{\gamma}_0 \left\langle \frac{|\tau_\xi| - \tau_\mathrm{C}}{\tau_\mathrm{D}} \right\rangle^m \operatorname{sgn}(\tau_\xi) \right| = \dot{\gamma}_0 \sum_{\xi=1}^{N} \left\langle \frac{|\tau_\xi| - \tau_\mathrm{C}}{\tau_\mathrm{D}} \right\rangle^m . \tag{A6}$$

A.2 Multiphase-field—simplifications

A.2.1 Potential and gradient contribution of the free energy density

The contributions f_grad and f_pot are considered due to the regularization of an SI towards a diffuse interface, reading

$$f_\mathrm{grad}(\boldsymbol{\phi}, \nabla\boldsymbol{\phi}) = \epsilon \sum_{\beta=2}^{N^*} \sum_{\alpha=1}^{\beta-1} \gamma_{\alpha\beta} \left| \phi_\alpha \operatorname{grad}(\phi_\beta) - \phi_\beta \operatorname{grad}(\phi_\alpha) \right|^2 , \tag{A7}$$

as well as

$$f_\mathrm{pot}(\boldsymbol{\phi}) = \frac{16}{\epsilon\pi^2} \sum_{\beta=2}^{N^*} \sum_{\alpha=1}^{\beta-1} \gamma_{\alpha\beta} \phi_\alpha \phi_\beta + \frac{1}{\epsilon} \sum_{\delta=3}^{N^*} \sum_{\beta=2}^{\delta-2} \sum_{\alpha=1}^{\beta-1} \gamma_{\alpha\beta\delta} \phi_\alpha \phi_\beta \phi_\delta \tag{A8}$$

cf., e.g., [73]. The contribution f_pot according to Eq. (A8) is referred to as multi-obstacle potential. In this context, if the n-tuple $\boldsymbol{\phi} = \{\phi_1, \ldots, \phi_{N^*}\}$ is not within the Gibbs simplex, given by

$$\mathcal{G} = \left\{ \boldsymbol{\phi} : \sum_{\alpha=1}^{N^*} \phi_\alpha(\boldsymbol{x}, t) = 1,\ \phi_\alpha \geq 0 \,\forall\alpha \right\}, \tag{A9}$$

cf., e.g., [57, Eq. (7)], $f_\mathrm{pot} = \infty$ is enforced. The parameter $\gamma_{\alpha\beta}$ refers to the interfacial energy between phases α and β, while the parameter $\gamma_{\alpha\beta\delta}$ prevents the formation of any third phase in a two-phase region, cf., e.g., [90]. The parameter ϵ is associated with the width of an interface in equilibrium which is given by $L_\delta = \pi^2\epsilon/4$.

A.2.2 Evolution equation and driving forces

The evolution equation of the order parameter is obtained by

$$\frac{\partial\phi_\alpha}{\partial t} = -\frac{1}{\epsilon\tilde{N}} \sum_{\beta=1,\beta\neq\alpha}^{\tilde{N}} M_{\alpha\beta} \left(\frac{\delta f}{\delta\phi_\alpha} - \frac{\delta f}{\delta\phi_\beta} \right), \tag{A10}$$

cf., e.g., [72], where $\tilde{N}$ denotes the number of locally present phases. Here, the variational derivative $\delta f/\delta\phi_\alpha$ is introduced as, e.g., in [91, Eqs. (13.63)&(13.64)], reading

$$\frac{\delta f}{\delta\phi_\alpha} = \left(\frac{\partial f}{\partial\phi_\alpha} - \operatorname{div}\left(\frac{\partial f}{\partial \operatorname{grad}(\phi_\alpha)} \right) \right) \tag{A11}$$

Introducing the notions of the mechanical driving force $\Delta^{\alpha\beta}_\mathrm{bulk}$ as well as the surface driving forces $\Delta^{\alpha\beta}_{\mathcal{S},\mathrm{p}}$ and $\Delta^{\alpha\beta}_{\mathcal{S},\mathrm{g}}$ as

$$\Delta^{\alpha\beta}_\mathrm{bulk} := \frac{\partial\overline{f}_\mathrm{bulk}}{\partial\phi_\alpha} - \frac{\partial\overline{f}_\mathrm{bulk}}{\partial\phi_\beta}, \tag{A12}$$

$$\Delta^{\alpha\beta}_{\mathcal{S},\mathrm{p}} := \frac{\partial\left(f_\mathrm{grad} + f_\mathrm{pot}\right)}{\partial\phi_\alpha} - \frac{\partial\left(f_\mathrm{grad} + f_\mathrm{pot}\right)}{\partial\phi_\beta}, \tag{A13}$$

$$\Delta^{\alpha\beta}_{\mathcal{S},\mathrm{g}} := \operatorname{div}\left(\frac{\partial f_\mathrm{grad}}{\partial \operatorname{grad}(\phi_\alpha)} \right) - \operatorname{div}\left(\frac{\partial f_\mathrm{grad}}{\partial \operatorname{grad}(\phi_\beta)} \right) \tag{A14}$$

the evolution equation of the order parameter according to Eq. (A10) reads

$$\frac{\partial\phi_\alpha}{\partial t} = -\frac{1}{\epsilon\tilde{N}} \sum_{\beta=1,\beta\neq\alpha}^{\tilde{N}} M_{\alpha\beta} \left(\Delta^{\alpha\beta}_\mathrm{bulk} + \Delta^{\alpha\beta}_{\mathcal{S},\mathrm{p}} - \Delta^{\alpha\beta}_{\mathcal{S},\mathrm{g}} \right). \tag{A15}$$

The simplifications carried out in the following paragraph, yield a compact form of the driving forces arising from the

free energy density $\overline{f}_{\text{bulk}}$, reading

$$\Delta^{\alpha\beta}_{\text{bulk}} = \{f_{\text{e}}\}^{\alpha\beta} + \{f_{\text{p}}\}^{\alpha\beta} - \Delta^{\alpha\beta}_{\sigma}, \tag{A16}$$

$$\Delta^{\alpha\beta}_{\sigma} = \sum_{\gamma\neq\alpha} \left(\phi_\gamma \boldsymbol{\sigma}^\gamma \cdot \{\boldsymbol{H}\}^{\alpha\gamma}\right) - \sum_{\gamma\neq\beta} \left(\phi_\gamma \boldsymbol{\sigma}^\gamma \cdot \{\boldsymbol{H}\}^{\beta\gamma}\right), \tag{A17}$$

which yields after further manipulations, carried out in a subsequent paragraph,

$$\Delta^{\alpha\beta}_{\text{bulk}} = \{f_{\text{e}}\}^{\alpha\beta} + \{f_{\text{p}}\}^{\alpha\beta} - \overline{\boldsymbol{\sigma}} \cdot \left(\{\boldsymbol{H}\}^{1\beta} - \{\boldsymbol{H}\}^{1\alpha}\right). \tag{A18}$$

A.2.3 Calculation of the mechanical driving force

Regarding the derivation of the evolution equation, the partial derivative of the free energy density with respect to the order parameter affects the contributions f_{grad}, f_{pot}, and $\overline{f}_{\text{bulk}}$, i.e.,

$$\frac{\partial f}{\partial \phi_\alpha} = \frac{\partial \left(f_{\text{grad}} + f_{\text{pot}} + \overline{f}_{\text{bulk}}\right)}{\partial \phi_\alpha} \tag{A19}$$

holds true. Since the phase-wise strains $\boldsymbol{\varepsilon}^\alpha$ depends on the order parameters, the contributions $f_{\text{e},\alpha}$ also also depends on the order parameters. Consequently, the derivative of $\overline{f}_{\text{bulk}}$ with respect to the order parameter requires the application of the chain rule, leading to

$$\frac{\partial \overline{f}_{\text{bulk}}}{\partial \phi_\alpha} = f_{\text{e},\alpha} + \sum_\beta \left(\phi_\beta \frac{\partial f_{\text{e},\beta}}{\partial \phi_\alpha}\right) + f_{\text{p},\alpha}, \quad \frac{\partial f_{\text{e},\beta}}{\partial \phi_\alpha} = \frac{\partial f_{\text{e},\beta}}{\partial \boldsymbol{\varepsilon}^\beta} \cdot \frac{\partial \boldsymbol{\varepsilon}^\beta}{\partial \phi_\alpha} \tag{A20}$$

Taking into account Eq. (11), the partial derivative $\partial \boldsymbol{\varepsilon}^\beta / \partial \phi_\alpha$ can be written as

$$\frac{\partial \boldsymbol{\varepsilon}^\beta}{\partial \phi_\alpha} = \sum_{\delta\neq\beta} \frac{\partial \phi_\delta}{\partial \phi_\alpha} \{\boldsymbol{\varepsilon}\}^{\beta\delta} = \{\boldsymbol{\varepsilon}\}^{\beta\alpha}, \quad \frac{\partial \boldsymbol{\varepsilon}^\beta}{\partial \phi_\alpha} = \{\boldsymbol{\varepsilon}\}^{\beta\alpha} \tag{A21}$$

Moreover, taking into account $\partial f_{\text{e},\beta} / \partial \boldsymbol{\varepsilon}^\beta = \boldsymbol{\sigma}^\beta$, Eq. (A20) reads

$$\frac{\partial \overline{f}_{\text{bulk}}}{\partial \phi_\alpha} = f_{\text{e},\alpha} + \sum_{\beta\neq\alpha} \left(\phi_\beta \boldsymbol{\sigma}^\beta \cdot \{\boldsymbol{\varepsilon}\}^{\beta\alpha}\right) + f_{\text{p},\alpha} \tag{A22}$$

Taking into account the symmetry of $\boldsymbol{\sigma}$ as well as Eq. (9),

$$\boldsymbol{\sigma}^\beta \cdot \{\boldsymbol{\varepsilon}\}^{\beta\alpha} = -\boldsymbol{\sigma}^\beta \cdot \{\boldsymbol{H}\}^{\alpha\beta} \tag{A23}$$

holds true. Thus, Eq. (A22) can be written as

$$\frac{\partial \overline{f}_{\text{bulk}}}{\partial \phi_\alpha} = f_{\text{e},\alpha} - \sum_{\beta\neq\alpha} \left(\phi_\beta \boldsymbol{\sigma}^\beta \cdot \{\boldsymbol{H}\}^{\alpha\beta}\right) + f_{\text{p},\alpha} \tag{A24}$$

For a better readibility, the summation index is changed to γ. Thus, the derivatives of $\overline{f}_{\text{bulk}}$ with respect to α and β are given by

$$\frac{\partial \overline{f}_{\text{bulk}}}{\partial \phi_\alpha} = f_{\text{e},\alpha} - \sum_{\gamma\neq\alpha} \left(\phi_\gamma \boldsymbol{\sigma}^\gamma \cdot \{\boldsymbol{H}\}^{\alpha\gamma}\right) + f_{\text{p},\alpha},$$

$$\frac{\partial \overline{f}_{\text{bulk}}}{\partial \phi_\beta} = f_{\text{e},\beta} - \sum_{\gamma\neq\beta} \left(\phi_\gamma \boldsymbol{\sigma}^\gamma \cdot \{\boldsymbol{H}\}^{\beta\gamma}\right) + f_{\text{p},\beta} \tag{A25}$$

By means of Eq. (A25), the mechanical driving force according to Eq. $(A14)_1$ can be written as

$$\Delta^{\alpha\beta}_{\text{bulk}} = \{f_{\text{e}}\}^{\alpha\beta} + \{f_{\text{p}}\}^{\alpha\beta} - \Delta^{\alpha\beta}_{\sigma},$$

$$\Delta^{\alpha\beta}_{\sigma} = \sum_{\gamma\neq\alpha} \left(\phi_\gamma \boldsymbol{\sigma}^\gamma \cdot \{\boldsymbol{H}\}^{\alpha\gamma}\right) - \sum_{\gamma\neq\beta} \left(\phi_\gamma \boldsymbol{\sigma}^\gamma \cdot \{\boldsymbol{H}\}^{\beta\gamma}\right) \tag{A26}$$

A.2.4 Simplification of the mechanical driving force

Regarding the implementation, the contribution $\Delta^{\alpha\beta}_{\sigma}$ of Eq. (A26) can be simplified as illustrated in the following.

$$\begin{aligned}\Delta^{\alpha\beta}_{\sigma} &= \phi_\beta \boldsymbol{\sigma}^\beta \cdot \{\boldsymbol{H}\}^{\alpha\beta} + \sum_{\gamma\neq\alpha\neq\beta} \left(\phi_\gamma \boldsymbol{\sigma}^\gamma \cdot \{\boldsymbol{H}\}^{\alpha\gamma}\right) \\ &\quad - \phi_\alpha \boldsymbol{\sigma}^\alpha \cdot \{\boldsymbol{H}\}^{\beta\alpha} - \sum_{\gamma\neq\alpha\neq\beta} \left(\phi_\gamma \boldsymbol{\sigma}^\gamma \cdot \{\boldsymbol{H}\}^{\beta\gamma}\right) \qquad \text{(A27)} \\ &= \sum_{\gamma\neq\alpha\neq\beta} \left(\phi_\gamma \boldsymbol{\sigma}^\gamma \cdot \left(\{\boldsymbol{H}\}^{\alpha\gamma} - \{\boldsymbol{H}\}^{\beta\gamma}\right)\right) \\ &\quad + \left(\phi_\beta \boldsymbol{\sigma}^\beta + \phi_\alpha \boldsymbol{\sigma}^\alpha\right) \cdot \{\boldsymbol{H}\}^{\alpha\beta} \qquad \text{(A28)}\end{aligned}$$

Accounting for $\{\psi\}^{\alpha\gamma} - \{\psi\}^{\beta\gamma} = \psi^\alpha - \psi^\gamma - \psi^\beta + \psi^\gamma = \{\psi\}^{\alpha\beta}$, Eq. (A28) can be rewritten as

$$\Delta^{\alpha\beta}_{\sigma} = \left(\sum_{\gamma\neq\alpha\neq\beta} \phi_\gamma \boldsymbol{\sigma}^\gamma\right) \cdot \{\boldsymbol{H}\}^{\alpha\beta} + \left(\phi_\beta \boldsymbol{\sigma}^\beta + \phi_\alpha \boldsymbol{\sigma}^\alpha\right) \cdot \{\boldsymbol{H}\}^{\alpha\beta} \tag{A29}$$

$$= \left(\sum_\gamma \phi_\gamma \boldsymbol{\sigma}^\gamma\right) \cdot \{\boldsymbol{H}\}^{\alpha\beta} = \overline{\boldsymbol{\sigma}} \cdot \{\boldsymbol{H}\}^{\alpha\beta} \tag{A30}$$

Taking into account

$$\boldsymbol{H}^\alpha = \boldsymbol{H}^1 - \boldsymbol{a}^{1\alpha} \otimes \boldsymbol{n}^{1\alpha} \phi_\alpha, \tag{A31}$$

cf., e.g., [74, Eq. (8)], Eq. (A30) can be simplified as following

$$\Delta_{\sigma}^{\alpha\beta} = \overline{\boldsymbol{\sigma}} \cdot \left(\boldsymbol{H}^{\alpha} - \boldsymbol{H}^{\beta}\right) = \overline{\boldsymbol{\sigma}} \cdot \Big(\boldsymbol{H}^{1} - \boldsymbol{a}^{1\alpha} \otimes \boldsymbol{n}^{1\alpha} \phi_{\alpha} - \left(\boldsymbol{H}^{1} - \boldsymbol{a}^{1\beta} \otimes \boldsymbol{n}^{1\beta} \phi_{\beta}\right)\Big) \tag{A32}$$

$$= \overline{\boldsymbol{\sigma}} \cdot \left(\boldsymbol{a}^{1\beta} \otimes \boldsymbol{n}^{1\beta} \phi_{\beta} - \boldsymbol{a}^{1\alpha} \otimes \boldsymbol{n}^{1\alpha} \phi_{\alpha}\right) = \overline{\boldsymbol{\sigma}} \cdot \left(\{\boldsymbol{H}\}^{1\beta} - \{\boldsymbol{H}\}^{1\alpha}\right). \tag{A33}$$

Consequently, the mechanical driving force according to Eq. (A26) reads

$$\Delta_{\text{bulk}}^{\alpha\beta} = \{f_{\text{e}}\}^{\alpha\beta} + \{f_{\text{p}}\}^{\alpha\beta} - \overline{\boldsymbol{\sigma}} \cdot \left(\{\boldsymbol{H}\}^{1\beta} - \{\boldsymbol{H}\}^{1\alpha}\right). \tag{A34}$$

References

1. von Mises R (1928) Mechanik der plastischen Formänderung von Kristallen. ZAMM-J Appl Math Mech 8(3):161–185
2. Hill R, Orowan E (1948) A theory of the yielding and plastic flow of anisotropic metals. Proc R Soc Lond A 193(1033):281–297
3. Asaro RJ (1983) Crystal plasticity. J Appl Mech 50(4b):921–934
4. Kocks UF, Mecking H (2003) Physics and phenomenology of strain hardening: the FCC case. Prog Mater Sci 48(3):171–273
5. Rice JR (1971) Inelastic constitutive relations for solids: an internal-variable theory and its application to metal plasticity. J Mech Phys Solids 19(6):433–455
6. Bachurin DV, Weygand D, Gumbsch P (2010) Dislocation-grain boundary interaction in <111> textured thin metal films. Acta Mater 58(16):5232–5241
7. Fan H, Zhu Y, El-Awady JA, Raabe D (2018) Precipitation hardening effects on extension twinning in magnesium alloys. Int J Plast 106:186–202
8. Fan H, Ngan AHW, Gan K, El-Awady JA (2018) Origin of double-peak precipitation hardening in metallic alloys. Int J Plast 111:152–167
9. Stricker M, Gagel J, Schmitt S, Schulz K, Weygand D, Gumbsch P (2015) On slip transmission and grain boundary yielding. Meccanica 51(2):271–278
10. Chatterjee S, Li Y, Po G (2021) A discrete dislocation dynamics study of precipitate bypass mechanisms in nickel-based superalloys. Int J Plast 145:103062
11. Lu S, Kan Q, Zaiser M, Li Z, Kang G, Zhang X (2022) Size-dependent yield stress in ultrafine-grained polycrystals: A multi-scale discrete dislocation dynamics study. Int J Plast 149:103183
12. Hochrainer T (2016) Thermodynamically consistent continuum dislocation dynamics. J Mech Phys Solids 88:12–22
13. Schulz K, Sudmanns M, Gumbsch P (2017) Dislocation-density based description of the deformation of a composite material. Modell Simul Mater Sci Eng 25(6):064003
14. Schulz K, Wagner L, Wieners C (2019) A mesoscale continuum approach of dislocation dynamics and the approximation by a Runge–Kutta discontinuous Galerkin method. Int J Plast 120:248–261
15. Erdle H, Böhlke T (2017) A gradient crystal plasticity theory for large deformations with a discontinuous accumulated plastic slip. Comput Mech 60(6):923–942
16. Grilli N, Janssens KGF, Nellessen J, Sandlöbes S, Raabe D (2018) Multiple slip dislocation patterning in a dislocation-based crystal plasticity finite element method. Int J Plast 100:104–121
17. Ziemann M, Chen Y, Kraft O, Bayerschen E, Wulfinghoff S, Kirchlechner C, Tamura N, Böhlke T, Walter M, Gruber PA (2015) Deformation patterns in cross-sections of twisted bamboo-structured Au microwires. Acta Mater 97:216–222
18. Bayerschen E, Prahs A, Wulfinghoff S, Ziemann M, Gruber PA, Walter M, Böhlke T (2016) Modeling contrary size effects of tensile- and torsion-loaded oligocrystalline gold microwires. J Mater Sci 51(16):7451–7470
19. Maugin GA (2017) Non-classical continuum mechanics: a dictionary. Springer, Singapore
20. Prahs A, Böhlke T (2019) On interface conditions on a material singular surface. Continuum Mech Thermodyn 32:1417–1434
21. Khan AS, Liu J, Yoon JW, Nambori R (2015) Strain rate effect of high purity aluminum single crystals: experiments and simulations. Int J Plast 67:39–52
22. Khan AS, Liu J (2016) A deformation mechanism based crystal plasticity model of ultrafine-grained/nanocrystalline FCC polycrystals. Int J Plast 86:56–69
23. Cyr ED, Mohammadi M, Mishra RK, Inal K (2015) A three dimensional (3D) thermo-elasto-viscoplastic constitutive model for FCC polycrystals. Int J Plast 70:166–190
24. Cyr E, Mohammadi M, Brahme A, Mishra RK, Inal K (2017) Modeling the formability of aluminum alloys at elevated temperatures using a new thermo-elasto-viscoplastic crystal plasticity framework. Int J Mech Sci 128–129:312–325
25. Asim UB, Siddiq MA, Kartal ME (2019) A CPFEM based study to understand the void growth in high strength dual-phase titanium alloy (Ti-10V-2Fe-3Al). Int J Plast 122:188–211
26. Habib SA, Lloyd JT, Meredith CS, Khan AS, Schoenfeld SE (2019) Fracture of an anisotropic rare-earth-containing magnesium alloy (ZEK100) at different stress states and strain rates: Experiments and modeling. Int J Plast 122:285–318
27. Su Y, Han QN, Qiu W, He Z, Shang YB, Shi HJ et al (2020) High temperature in-situ SEM observation and crystal plasticity simulation on fretting fatigue of Ni-based single crystal superalloys. Int J Plast 127:102645
28. Hollenweger Y, Kochmann DM (2022) An efficient temperature-dependent crystal plasticity framework for pure magnesium with emphasis on the competition between slip and twinning. Int J Plast 159:103448
29. Connolly DS, Kohar CP, Inal K (2022) A novel crystal plasticity model incorporating transformation induced plasticity for a wide range of strain rates and temperatures. Int J Plast 152:103188
30. Bonatti C, Berisha B, Mohr D (2022) From CP-FFT to CP-RNN: Recurrent neural network surrogate model of crystal plasticity. Int J Plast 158:103430
31. Gurtin ME (2000) On the plasticity of single crystals: free energy, microforces, plastic-strain gradients. J Mech Phys Solids 48(5):989–1036
32. Gurtin ME (2002) A gradient theory of single-crystal viscoplasticity that accounts for geometrically necessary dislocations. J Mech Phys Solids 50(1):5–32
33. Ryś M, Forest S, Petryk H (2020) A micromorphic crystal plasticity model with the gradient-enhanced incremental hardening law. Int J Plast 128:102655
34. Gurtin ME (2008) A theory of grain boundaries that accounts automatically for grain misorientation and grain-boundary orientation. J Mech Phys Solids 56(2):640–662
35. Wulfinghoff S, Bayerschen E, Böhlke T (2013) A gradient plasticity grain boundary yield theory. Int J Plast 51:33–46
36. Wulfinghoff S (2017) A generalized cohesive zone model and a grain boundary yield criterion for gradient plasticity derived from surface- and interface-related arguments. Int J Plast 92:57–78

37. Moelans N, Blanpain B, Wollants P (2008) An introduction to phase-field modeling of microstructure evolution. Calphad Comput Coupling Phase Diagrams Thermochem 32(2):268–294
38. Steinbach I (2009) Phase-field models in materials science. Modell Simul Mater Sci Eng 17(7):073001
39. Nestler B, Choudhury A (2011) Phase-field modeling of multi-component systems. Curr Opin Solid State Mater Sci 15(3):93–105
40. Levitas VI, Roy AM (2016) Multiphase phase field theory for temperature-induced phase transformations: formulation and application to interfacial phases. Acta Mater 105:244–257
41. Chen LQ (2002) Phase-field models for microstructure evolution. Annu Rev Mater Res 32(1):113–140
42. Steinbach I (2013) Phase-field model for microstructure evolution at the mesoscopic scale. Annu Rev Mater Res 43(1):89–107
43. Ali MA, Shchyglo O, Stricker M, Steinbach I (2023) Coherency loss marking the onset of degradation in high temperature creep of superalloys: phase-field simulation coupled to strain gradient crystal plasticity. Comput Mater Sci 220:112069
44. Güvenç O, Henke T, Laschet G, Böttger B, Apel M, Bambach M, Hirt G (2013) Modeling of static recrystallization kinetics by coupling crystal plasticity FEM and multiphase field calculations. Comput Methods Mater Sci 13(2):368–374
45. Güvenç O, Bambach M, Hirt G (2014) Coupling of crystal plasticity finite element and phase field methods for the prediction of SRX kinetics after hot working. Steel Res Int 85(6):999–1009
46. Ammar K, Appolaire B, Cailletaud G, Forest S (2009) Combining phase field approach and homogenization methods for modelling phase transformation in elastoplastic media. Eur J Comput Mech/Revue Européenne de Mécanique Numérique. 18(5–6):485–523
47. de Rancourt V, Ammar K, Appolaire B, Forest S (2016) Homogenization of viscoplastic constitutive laws within a phase field approach. J Mech Phys Solids 88:291–319
48. Willis JR (1981) Variational and related methods for the overall properties of composites. Adv Appl Mech 21:1–78
49. Torquato S (2002) Random heterogeneous materials: microstructure and macroscopic properties. Interdisciplinary applied mathematics; 16. Springer, New York
50. Dvorak GJ, Dvorak G (2013) Micromechanics of composite materials. Solid mechanics and its applications, vol 186. Springer, Dordrecht
51. Hill R (1963) Elastic properties of reinforced solids: some theoretical principles. J Mech Phys Solids 11(5):357–372
52. Durga A, Wollants P, Moelans N (2013) Evaluation of interfacial excess contributions in different phase-field models for elastically inhomogeneous systems. Modell Simul Mater Sci Eng 21(5):055018
53. Mosler J, Shchyglo O, Montazer Hojjat H (2014) A novel homogenization method for phase field approaches based on partial rank-one relaxation. J Mech Phys Solids 68:251–266
54. Schneider D, Schwab F, Schoof E, Reiter A, Herrmann C, Selzer M, Böhlke T, Nestler B (2017) On the stress calculation within phase-field approaches: a model for finite deformations. Comput Mech 60(2):203–217
55. Svendsen B, Shanthraj P, Raabe D (2018) Finite-deformation phase-field chemomechanics for multiphase, multicomponent solids. J Mech Phys Solids 112:619–636
56. Schneider D, Tschukin O, Choudhury A, Selzer M, Böhlke T, Nestler B (2015) Phase-field elasticity model based on mechanical jump conditions. Comput Mech 55(5):887–901
57. Schneider D, Schoof E, Tschukin O, Reiter A, Herrmann C, Schwab F, Selzer M, Nestler B (2018) Small strain multiphase-field model accounting for configurational forces and mechanical jump conditions. Comput Mech 61(3):277–295
58. Müller I (1985) Thermodynamics. Pitman, Boston
59. Cermelli P, Fried E, Gurtin ME (2005) Transport relations for surface integrals arising in the formulation of balance laws for evolving fluid interfaces. J Fluid Mech 544:339–351
60. Prahs A, Böhlke T (2019) On invariance properties of an extended energy balance. Continuum Mech Thermodyn 32:843–859
61. Maugin GA (1992) The thermomechanics of plasticity and fracture. Cambridge University Press, Cambride
62. Prahs A, Böhlke T (2021) The role of dissipation regarding the concept of purely mechanical theories in plasticity. Mech Res Commun 119:103832
63. Evers L, Brekelmans W, Geers M (2004) Non-local crystal plasticity model with intrinsic SSD and GND effects. J Mech Phys Solids 52(10):2379–2401
64. Perzyna P (1971) Thermodynamic theory of viscoplasticity. Adv Appl Mech 1:313–354
65. Patel NR, Bieniek MP (1979) An analysis of the viscoplastic behavior of metals. Mater Sci Eng 40(1):123–134
66. Sung JH, Kim JH, Wagoner RH (2010) A plastic constitutive equation incorporating strain, strain-rate, and temperature. Int J Plast 26(12):1746–1771
67. Wulfinghoff S (2014) Numerically efficient gradient crystal plasticity with a grain boundary yield criterion and dislocation-based work-hardening. KIT Scientific Publishing, Schriftenreihe Kontinuumsmechanik im Maschinenbau Nr. 5. Karlsruhe
68. Bayerschen E (2017) Single-crystal gradient plasticity with an accumulated plastic slip: theory and applications. KIT Scientific Publishing, Schriftenreihe Kontinuumsmechanik im Maschinenbau Nr. 9. Karlsruhe
69. Gurtin ME, Fried E, Anand L (2010) The mechanics and thermodynamics of continua. Cambridge University Press, Cambridge
70. Miehe C, Schröder J (2001) A comparative study of stress update algorithms for rate-independent and rate-dependent crystal plasticity. Int J Numer Methods Eng 50(2):273–298
71. Steinbach I, Pezzolla F, Nestler B, Seeßelberg M, Prieler R, Schmitz GJ, Rezende JLL (1996) A phase field concept for multiphase systems. Physica D 94(3):135–147
72. Steinbach I, Pezzolla F (1999) A generalized field method for multiphase transformations using interface fields. Physica D 134(4):385–393
73. Nestler B, Garcke H, Stinner B (2005) Multicomponent alloy solidification: phase-field modeling and simulations. Phys Rev E 71(4):041609
74. Herrmann C, Schoof E, Schneider D, Schwab F, Reiter A, Selzer M, Nestler B (2018) Multiphase-field model of small strain elasto-plasticity according to the mechanical jump conditions. Comput Mech 62(6):1399–1412
75. Šilhavý M (1997) The mechanics and thermodynamics of continuous media. Springer, Berlin
76. Ammar K, Appolaire B, Forest S, Cottura M, Le Bouar Y, Finel A (2014) Modelling inheritance of plastic deformation during migration of phase boundaries using a phase field method. Meccanica 49(11):2699–2717
77. Abrivard G, Busso EP, Forest S, Appolaire B (2012) Phase field modelling of grain boundary motion driven by curvature and stored energy gradients. Part I: theory and numerical implementation. Philos Mag 92(28–30):3618–3642
78. Simo J, Hughes T (2008) Computational inelasticity. Springer, New York
79. Zienkiewicz OC, Taylor RL (2000) The finite element method. vol. 2: Solid mechanics. Butterworth-Heinemann, Oxford
80. Simo JC, Taylor RL (1985) Consistent tangent operators for rate-independent elastoplasticity. Comput Methods Appl Mech Eng 48(1):101–118
81. Hughes TJ, Pister KS (1978) Consistent linearization in mechanics of solids and structures. Comput Struct 8(3):391–397

82. Bertram A (2005) Elasticity and plasticity of large deformations: an introduction. Springer, Berlin
83. Schwab FK, Reiter A, Herrmann C, Schneider D, Nestler B (2020) Phase-inherent linear visco-elasticity model for infinitesimal deformations in the multiphase-field context. Adv Model Simul Eng Sci 7(1):1–32
84. Hötzer J, Reiter A, Hierl H, Steinmetz P, Selzer M, Nestler B (2018) The parallel multi-physics phase-field framework Pace3D. J Comput Sci 26:1–12
85. Bayerschen E, Stricker M, Wulfinghoff S, Weygand D, Böhlke T (2015) Equivalent plastic strain gradient plasticity with grain boundary hardening and comparison to discrete dislocation dynamics. Proc R Soc A 471:1–19
86. Nikravesh PE (1988) Computer-aided analysis of mechanical systems. Prentice-Hall, Inc, Upper Saddle River
87. Prahs A, Reder M, Schneider D, Nestler B (2023) Thermomechanically coupled theory in the context of the multiphase-field method. Int J Mech Sci 257:108484
88. Coleman BD, Noll W (1963) The thermodynamics of elastic materials with heat conduction and viscosity. Arch Ration Mech Anal 13(1):167–178
89. Bertram A, Glüge R (2015) Solid mechanics: theory, modeling, and problems. Springer, Heidelberg
90. Hötzer J, Tschukin O, Said MB, Berghoff M, Jainta M, Barthelemy G, Smorchkov N, Schneider D, Selzer M, Nestler B (2016) Calibration of a multi-phase field model with quantitative angle measurement. J Mater Sci 51(4):1788–1797
91. Goldstein H, Poole CP, Safko JL (2002) Classical mechanics. Addison Wesley, San Francisco